UNIVERSITY OF CALIFORNIA SAN DIEGO

Parkinson's Disease-Linked LRRK2 Structure and Model for Microtubule Interaction

A dissertation submitted in partial satisfaction of the
requirements for the degree Doctor of Philosophy

in

Chemistry

by

Colin Deniston

Committee in charge:

Professor Andres Leschziner, Chair
Professor Susan Taylor, Co-Chair
Professor Rommie Amaro
Professor Samara Reck-Peterson
Professor Jerry Yang

2020

The Dissertation of Colin Deniston is approved, and it is acceptable in quality and form for publication on microfilm and electronically:

_____

_____

_____

_____
Co-Chair

_____
Chair

University of California San Diego

2020

DEDICATION

I want to dedicate this work to my best friend and partner Irene Bonner. Thank you for being my pillar of support and love through these 5 years. Without your snap pea sandwiches those long days and nights would have been impossible! Let this be the end to another chapter in the adventure of our lives together.

I would also like to dedicate this work to my mother, Nan Deniston, and father, Marty Deniston, who have always assisted and supported my endeavors in the scientific field. You've inspired me to never stop learning and helping the world through scientific discovery.

EPIGRAPH

I must not fear.
Fear is the mind-killer.
Fear is the little-death that brings total obliteration.
I will face my fear.
I will permit it to pass over me and through me.
And when it has gone past, I will turn the inner eye to see its path.
Where the fear has gone there will be nothing. Only I will remain.

Dune: Frank Herbert

TABLE OF CONTENTS

LIST OF FIGURES

LIST OF SUPPLEMENTAL FILES

Extended Data Video 1: LRRK2^{RCKW} Structure. Overview of the cryo-EM structure of LRRK2^{RCKW} with close-ups of its domains.

Extended Data Video 2: Parkinson's Disease mutations in LRRK2^{RCKW} Structure. Close-ups of the residues most commonly mutated in PD. I2020 (mutated to T2020 in PD) is disordered in our structure and this is indicated by the square brackets around its name.

Extended Data Video 3: The C-terminal helix of LRRK2^{RCKW}. Close-up of the C-terminal helix of LRRK2^{RCKW} showing the residues involved in electrostatic and hydrophobic interactions between it and the kinase domain.

ACKNOWLEDGEMENTS

I would like to acknowledge Professor Andres Leschziner for his support as chair and mentor over these past years. His guidance has helped shape my research into the tremendous body of work it is today.

I would also like to acknowledge Professor Samara Reck-Peterson for her mentorship and supervision with this work. The impact of this work would have never been what it is without your lab's single molecule and cellular findings relating the cryo-EM structure to human biology.

I would like to acknowledge Professor Susan Taylor as well for her role in beginning and fueling so many Parkinson's related collaborations here at UC San Diego. Her effort has helped make UC San Diego a global leader in the biochemistry of LRRK2-associated Parkinson's Disease research.

I would also like to acknowledge the post-docs John Salogiannis, David Snead, and Indrajit Lahiri for all the tremendous work they put into this research as well as the guidance they have given me.

Chapter 1, in full, is a reprint of material as it appears in Parkinson's Disease-Linked LRRK2 Structure and Model for Microtubule Interaction, 2020. Colin K. Deniston, John Salogiannis, Sebastian Mathea, David M. Snead, Indarjit Lahiri, Oscar Donosa, Reika Watanabe, Jan Böhning, Andrew K. Shiau, Stefan Knapp, Elizabeth Villa, Samara L. Reck-Peterson, Andres E. Leschziner., Nature, 2020. The dissertation author was a co-author of this paper.

VITA

2013 Bachelors of Science, University of California, Davis

2013 Research Associate II, Amunix Operating Inc.

2020 Doctor of Philosophy, University of California, San Diego

PUBLICATIONS

Colin K. Deniston, John Salogiannis, Sebastian Mathea, David M. Snead, Indarjit Lahiri, Oscar Donosa, Reika Watanabe, Jan Böhning, Andrew K. Shiau, Stefan Knapp, Elizabeth Villa, Samara L. Reck-Peterson, Andres E. Leschziner (2020). Parkinson's Disease-Linked LRRK2 Structure and Model for Microtubule Interaction. Under Review in Nature.

Sheng Ding, Michael Song, Bee-Cheng Sim, Chen Gu, Vladimir N. Podust, Chia-Wei Wang, Bryant McLaughlin, Trishul P Shah, Rodney Lax, Rainer Gast, Rahul Sharan, Arthur Vasek, M. Amanda Hartman, Colin Deniston, Prathna Srinivas, and Volker Schellenberger (2014). Multivalent Antiviral XTEN-Peptide Conjugates with Long In Vivo Half-Live and Enhances Solubility. Bioconjugate Chem. 25(7):1351

ABSTRACT OF THE DISSERTATION

Parkinson's Disease-Linked LRRK2 Structure and Model for Microtubule Interaction

by

Colin Deniston

Doctor of Philosophy in Chemistry

University of California San Diego, 2020

Professor Andres Leschziner, Chair

Professor Susan Taylor, Co-Chair

Leucine Rich Repeat Kinase 2 (LRRK2) is the most commonly mutated gene in familial Parkinson's disease. LRRK2 is proposed to function in membrane trafficking and co-localizes with microtubules. We report the 3.5Å structure of the catalytic half of LRRK2, and an atomic

model of microtubule-associated LRRK2 built using a reported 14Å structure obtained by cryo-electron tomography. We propose that the conformation of LRRK2's kinase domain regulates its microtubule interaction, with a closed conformation favoring binding. We show that the catalytic half of LRRK2 is sufficient for microtubule binding and blocks the motility of the microtubule-based motors kinesin and dynein *in vitro*. Kinase inhibitors that stabilize an open conformation relieve this interference and reduce LRRK2 filament formation in cells, while those that stabilize a closed conformation do not. Our findings suggest that LRRK2 is a roadblock for microtubule-based motors and have implications for the design of therapeutic LRRK2 kinase inhibitors.

CHAPTER 1: Parkinson's Disease-Linked LRRK2 Structure and Model for Microtubule Interaction

INTRODUCTION

Mutations in Leucine-Rich Repeat Kinase 2 (LRRK2) are the most common cause of familial Parkinson's Disease (PD)[1]. LRRK2 is also linked to the idiopathic form of PD: mutations in LRRK2 are a genetic risk factor[1] and increased LRRK2 kinase activity is linked to disease[2]. A growing body of evidence suggests that mutations in LRRK2 are also risk factors for Crohn's Disease and leprosy[3-5]. Like many other PD-causing genes, LRRK2 is implicated in membrane trafficking[6]. Mutant LRRK2 causes defects in the trafficking of endosomes, lysosomes, autophagosomes, and mitochondria[6,7]. Furthermore, Rab GTPases, central regulators of membrane trafficking, are physiological substrates of LRRK2[8,9]. In cells, all five major PD-causing mutations increase the phosphorylation of LRRK2's Rab substrates[8,9]. Long-distance transport of Rab-marked membranes occurs along microtubules and is driven by the microtubule-based motors dynein and kinesin[10,11]. LRRK2 function and/or pathology has also been linked to microtubules as LRRK2 partially co-localizes with microtubules in cells[12] and four of the five major PD-causing mutations (Fig. 1a)[1] enhance microtubule association of LRRK2[13].

LRRK2 is a large (288 kDa) multi-domain protein. Its amino-terminal half is comprised of repetitive protein interaction motifs (Armadillo, Ankyrin, and Leucine-Rich Repeats) and its carboxy-terminal catalytic half contains a Ras-like GTPase (Ras-of-Complex, or RoC domain), a kinase domain, and two other domains (C-terminal Of Roc, or COR, and WD40) (Fig. 1a). Despite LRRK2's fundamental importance for understanding and treating PD, there is limited structural information on LRRK2. While structures are available for bacterial homologs of the LRR, RoC and COR domains[14,15], and a D. discoideum homolog of the kinase domain[16], the

only two high-resolution structures available for the human protein are for its RoC17 and WD40 domains[18] and no larger structures have been reported. Structures of the full-length protein obtained using negative stain[19] and cryo-electron microscopy (Cryo-EM)20 have been published, but their resolutions were limited (22Å and 16Å, respectively). A recent reconstruction of LRRK2 bound to microtubules in cells using cryo-electron tomography (Cryo-ET) and sub-tomogram averaging led to a 14Å structure and proposed model of the catalytic half of LRRK2[21]. Here, we set out to determine a high-resolution structure of LRRK2's catalytic half using cryo-EM, as well as to understand how it interacts with microtubules and how this impacts the movement of microtubule-based motors.

RESULTS

Cryo-EM structure of the catalytic half of LRRK2

High-resolution studies on human LRRK2 have been limited by the lack of efficient expression systems resulting in stable LRRK2 protein. We tested a large number of constructs (Extended Data Fig. 1a), leading to the identification of one consisting of the carboxy-terminal half of LRRK2 (amino acids 1,327 to 2,527), which expressed well in insect cells and resulted in a stable protein (Extended Data Fig. 1b, c). This construct comprises the RoC, COR, kinase and WD40 domains of LRRK2 (Fig. 1a), which we refer to as LRRK2^{RCKW}. The COR domain was previously defined as consisting of two subdomains, COR-A and COR-B, based on its structure from a bacterial homolog[14].

We determined a 3.5Å structure of LRRK2^{RCKW} in the presence of GDP using cryo-EM (Fig. 1b, c and Extended Data Fig. 2). On our grids, we observed a mixture of monomers, dimers and head-to-tail trimers and we used the trimer to solve the structure (Fig. 1b and Extended Data Fig. 2b). This trimer species was critical for reaching high resolution, but it is

likely specific to the EM grid preparation as LRRK2^{RCKW} is predominantly monomeric, with a smaller percentage of dimers, in solution (Extended Data Fig. 3). The RoC and COR-A domains were flexible in our structure, yielding significantly lower resolutions than the rest of the protein as a result of the symmetry imposed on the trimer (Fig. 1b, c). In order to improve the density of this part of the map, we used signal subtraction to generate LRRK2^{RCKW} trimers containing only one of the three RoC and COR-A domains and subjected those to 3D classification and refinement focused on the monomer containing RoC and COR-A. This resulted in a 3.8Å structure with improved local resolution for RoC and COR-A (Fig. 1d, e, Extended Data Fig. 2f-i). We used a combination of Rosetta[22] and manual building in coot[23] to generate the final model. The RoC and COR-A domains were built using the signal subtracted maps, and then combined with the COR-B, kinase and WD40 domains, which were built using the original higher resolution trimer map (Fig. 1f and Extended Data Video 1). Importantly, the atomic model of LRRK2^{RCKW} we obtained from the trimers fits well into a 8.1Å reconstruction of a LRRK2^{RCKW} monomer (Fig. 1g, h), indicating that formation of the trimer does not cause major structural changes in the protein.

LRRK2^{RCKW} adopts an overall J-shaped structure, with the WD40, kinase and COR-B domains arranged along one axis, and COR-A and RoC turning around back towards the kinase, bringing COR-A, and therefore the tightly associated RoC domain, which has GDP bound, in close proximity to the kinase's C-lobe (Fig. 1f, i and Extended Data Video 1). This arrangement likely underpins the reported crosstalk between LRRK2's kinase and GTPase[24,25] (reviewed in[26]). Part of the FERM domain in the FAK-FERM complex approaches the FAK C-lobe in a similar way[27] (Extended Data Fig. 4a, b). The RoC, COR-A and COR-B domains are arranged as previously seen in crystal structures of the COR[14], RoC-COR[14,28], and LRR-RoC-COR[15] fragments of bacterial homologs of LRRK2. The N-lobe of the LRRK2^{RCKW} kinase domain, in particular its αC helix, forms an extensive interaction with the COR-B domain, with

COR-B occupying a location reminiscent of that of Cyclin A in CDK2-Cyclin A29 (Extended Data Fig. 4a, c).

The kinase in LRRK2^{RCKW} is in an open, inactive conformation. Its activation loop is disordered beyond G2019, the location of one of the major familial PD mutations (G2019S) (Fig. 1j, k and Extended Data Video 2). Thus, I2020, the location of the other familial PD mutation found in the activation loop (I2020T), is disordered in our structure (Fig. 1j, k and Extended Data Video 2). R1441 and Y1699 are the sites of three other familial PD mutations and are located at the RoC-COR-B interface (Fig. 1j, k and Extended Data Video 2). Y2018 of the DYG motif (DFG motif in other kinases) forms a hydrogen bond with the backbone carbonyl of I1933 in the N-lobe (Extended Data Fig. 4j, k), providing a structural explanation for the hyperactivation of the kinase resulting from a Y2018F mutation[30], which would release the activation loop.

A unique feature of LRRK2 is a 28-amino acid α-helix located at its extreme C-terminus, following the WD40 domain (Fig. 1i, l, m and Extended Data Video 3). This helix extends along the entire kinase domain, interacting with both its C- and N-lobes (Fig. 1l, m and Extended Data Video 3). Deletion of this helix resulted in an insoluble protein (Extended Data Fig.1). While a number of other kinases have alpha helices in the same general location as LRRK2's C-terminal helix, none of those interactions are as extensive as that observed in LRRK2 (Extended Data Fig. 4d-i). A residue near its end (T2524) is a known phosphorylation site for LRRK2[31]. Given the close proximity between T2524 and the N-lobe of the kinase domain, as well as the adjacent COR-B domain, we hypothesize that phosphorylation of this residue may play a role in regulating the kinase. Since the last two residues of the C-terminal helix are disordered in our structure, as is a neighboring loop in COR-B, it is possible that conditions exist where these regions become ordered and turn the C-terminal helix into an anchoring element that connects COR-B, the kinase and the WD40 domain.

Although our construct lacks the N-terminal half of full-length LRRK2, we were able to model the Leucine-Rich Repeats (LRR) by using a recent crystal structure of the LRR, RoC, and

COR domains of C. tepidum's Roco protein, a bacterial homolog of LRRK2[15] (Extended Data Fig. 5a-e). Aligning the RoC and COR domains of this structure to those of LRRK2^{RCKW} resulted in a good fit for the LRR, which in the model wraps around the N-lobe of the kinase and comes in close proximity of its C-lobe as it connects to the RoC domain (Extended Data Fig. 5a-e). This model places the known S1292 autophosphorylation site in the LRR in close proximity to the kinase's active site, and the Crohn's disease-related residue N2081, located in the kinase's C-lobe adjacent to the LRR (Extended Data Fig. 5f), suggesting the functional relevance of this potential interface.

An atomic model of microtubule-bound LRRK2 filaments

Recently, a 14Å structure of microtubule-associated filaments of full-length LRRK2 (carrying the filament-promoting I2020T mutation13) was reported using *in situ* cryo-ET and sub-tomogram averaging[21] (Fig. 2a). The LRRK2 filaments formed on microtubules were right-handed[21]. The fact that microtubules are left-handed, combined with the absence of strong density connecting the LRRK2 filament to the microtubule surface[21] raised the question of whether LRRK2's interaction with microtubules is direct or is mediated by other microtubule-associated proteins. To address this, we combined purified microtubules with purified LRRK2^{RCKW} and observed them by cryo-EM. The resulting helical microtubule decoration (Fig. 2b) suggests that the interaction between LRRK2 and microtubules is direct and that the catalytic C-terminal half of LRRK2 is sufficient for the formation of microtubule-associated filaments.

Previously, integrative modeling was used to build a model into the *in situ* structure of microtubule-associated LRRK2[21]. This modeling indicated that the observed density was comprised of the RoC, COR, Kinase and WD40 domains and gave orientation ensembles for each domain[21] that were in good agreement with the high-resolution structure of LRRK2^{RCKW}

presented here. However, given the uncertainties in the domain orientations intrinsic to the integrative modeling approach, we set out to build an atomic model of the microtubule-bound LRRK2 filaments by combining our 3.5Å structure of LRRK2^{RCKW} with the 14Å *in situ* structure of microtubule-associated LRRK2. To guide model building, we took advantage of the characteristic shape of the WD40 domains, which are a prominent feature of the *in situ* structure (Fig. 2a and Extended Data Fig. 6a-c) and that a crystal structure of a WD40 dimer from LRRK2 was recently reported[18]. We first replaced the WD40 domains in the crystal structure with those from our LRRK2^{RCKW} structure (there are small differences between them) (Extended Data Fig. 6a) and then docked this WD40 dimer into the sub-tomogram average density (Extended Data Fig. 6b). Next, we aligned the LRRK2^{RCKW} structure to it, thus imposing the WD40 dimer interface from the crystal structure on our model (Extended Data Fig. 6d, e). This initial model revealed that the LRRK2^{RCKW} structure is sufficient to account for the density seen in the *in situ* structure (Fig. 2a, c), in agreement with our ability to reconstitute microtubule-associated LRRK2^{RCKW} filaments *in vitro* (Fig. 2b), and with the earlier integrative modeling[21]. The filaments formed *in vitro* with LRRK2^{RCKW} lack the regular pitch and spacing observed in cells (Fig. 2a, b); it is possible that other factors, such as the N-terminal half of LRRK2 or the nature of microtubules in cells, may play a role in establishing the precise geometry of the filaments.

Although the LRRK2^{RCKW} structure fits the overall shape of the sub-tomogram average, we noticed significant clashes at the filament interface formed by the COR domains (Fig. 2d, e). Since the kinase in our LRRK2^{RCKW} structure is in an open conformation (Fig. 2c), we wondered whether filament formation might require LRRK2's kinase to be in a closed conformation. We modeled a kinase-closed LRRK2^{RCKW} by running structural searches (DALI server) with either the N- or C-lobes of LRRK2^{RCKW}'s kinase and looked for a kinase in a closed conformation whose N- and C-lobes best matched those of LRRK2^{RCKW}. The top candidate was Interleukin-2 inducible T-cell kinase (ITK) (PDB: 3QGY). We aligned ITK to LRRK2^{RCKW} using the C-lobes of the two kinases, and then aligned the N-lobe of LRRK2^{RCKW}'s kinase to that of ITK, moving RoC,

COR-A and COR-B as a rigid body along with the kinase's N-lobe (Fig. 2f and Extended Data Fig. 6f-j). We then repeated the docking into the *in situ* structure, this time using the model of kinase-closed LRRK2^{RCKW}. In addition to improving the fit visually (Fig. 2g, h), using the kinase-closed LRRK2^{RCKW} model resolved more than 80% of the backbone clashes we had observed with our kinase-open LRRK2^{RCKW} structure (Fig. 2i). A closed conformation for the kinase had already been proposed by the earlier integrative modeling[21]. Given this data, we hypothesize that the conformation of LRRK2, as driven by the kinase, controls its ability to associate with microtubules, with a closed kinase promoting oligomerization, which increases binding, and an open (inactive) one disfavoring it (Fig. 2j, k).

The LRRK2 filaments in our kinase-closed model are formed by two types of homotypic interactions, each resulting in a two-fold axis of symmetry perpendicular to the microtubule axis: one is mediated by the WD40 domain, and the other by the COR-A and COR-B domains (Fig. 3a-d). Similar interfaces were reported based on integrative modeling performed with the 14Å LRRK2 structure obtained by cryo-ET[21]. We wondered whether these interfaces were specific to the microtubule-associated form of LRRK2. Additional structures we obtained from our cryo-EM data showed this was not the case; in addition to the trimers we used to obtain the 3.5Å structure of LRRK2^{RCKW}, grids prepared in the absence of microtubules also contained dimers that were mediated by the same two interfaces seen in the filaments (Fig. 3e, f and Extended Data Figs. 7-10). We observed these dimers under different conditions, both in the presence of kinase inhibitors as well as in their absence (Fig. 3e, f and Extended Data Fig. 10). All of our cryo-EM maps of dimers fit well the molecular models of dimers derived from the filaments, suggesting that the same interfaces observed off microtubules are involved in the formation of the microtubule-associated filaments.

Separately, we docked LRRK2^{RCKW}, split in half at the junction between the N- and C-lobes of the kinase, into the cryo-EM map of a WD40-mediated dimer obtained in the presence of MLi-2 (Extended Data Fig. 11a-c). We docked the resulting closed-kinase model of

LRRK2^{RCKW} (Extended Data Fig. 11e) into the cryo-EM maps of WD40- and COR-mediated dimers obtained in the presence of MLi-2 to generate molecular models of these dimers (Extended Data Fig. 11c, d-g). Finally, we aligned these models, in alternating order, to build a polymer *in silico*. The resulting structure was a right-handed helix with the same general geometric properties seen in the cellular LRRK2 filaments, indicating that those properties are largely encoded in the structure of LRRK2^{RCKW} itself (Fig. 3g-i and Extended Data Fig. 11g, h). Docking the same two halves of LRRK2^{RCKW} into the cryo-EM map of a monomer obtained in the absence of inhibitors led to a structure very similar to that obtained from the trimers, further confirming that formation of the trimer did not alter the conformation of LRRK2^{RCKW} (Extended Data Fig. 11a, b, d, e).

These data, along with the apparent lack of any residue-specific interactions between LRRK2 and the microtubule, suggest that the microtubule may be providing a surface for LRRK2 to oligomerize using interfaces that exist in solution. Consistent with this idea, the surface charge of the microtubule facing the LRRK2^{RCKW} filament is acidic, while there are a number of basic patches on the LRRK2^{RCKW} filament facing the microtubule (Extended Data Fig. 12). The unstructured C-terminal tails of α- and β-tubulin, which were not included in the surface charge calculations, are also acidic. Finally, the interface in the COR-mediated dimer we observed for LRRK2^{RCKW} differs from that reported for the homologous Roco protein from C. tepidum[14,15] (Extended Data Fig. 13). While the GTPase domains interact directly in the dimer of the bacterial protein[15], they are not involved in the dimerization interface of LRRK2 (Extended Data Fig. 13d, e).

LRRK2^{RCKW} inhibits kinesin and dynein motility *in vitro*

To test our hypothesis that the conformation of LRRK2's kinase domain regulates its interaction with microtubules, we needed a sensitive assay to measure the association of

LRRK2^{RCKW} with microtubules and a means to control the conformation of its kinase. Microtubule association was monitored by measuring the effect of LRRK2^{RCKW} on the movement of microtubule-based motors. We used a truncated dimeric human kinesin-1, Kif5B ("kinesin" here)[32], which moves towards the plus ends of microtubules, and activated human cytoplasmic dynein-1/ dynactin/ ninein-like complexes ("dynein" here) [33], which move in the opposite direction. Using single-molecule *in vitro* motility assays (Fig. 4a) we found that low nanomolar concentrations of LRRK2^{RCKW} inhibited both kinesin and dynein movement, with near complete inhibition achieved at 25 nM LRRK2^{RCKW} (Fig. 4b-e). We hypothesized that LRRK2^{RCKW} was acting as a roadblock for the motors. In agreement with this hypothesis, the run length of kinesin was reduced (Fig. 4f), while its velocity remained relatively constant (Fig. 4g). Activated cytoplasmic dynein-1 complexes also showed a significant reduction in run length in the presence of LRRK2^{RCKW} (Fig. 4h). Thus, LRRK2^{RCKW} robustly blocked the motility of both kinesin and dynein motors *in vitro*.

Ponatinib and GZD-824 rescue motor inhibition by LRRK2^{RCKW} *in vitro*

Our hypothesis predicts that the closed conformation of LRRK2's kinase domain will favor microtubule binding. Conversely, it predicts that conditions that stabilize the kinase in an open conformation will lead to decreased microtubule binding of LRRK2^{RCKW}, resulting in relief of LRRK2^{RCKW}-dependent inhibition of kinesin and dynein motility. To test these predictions, we searched for a Type 2 kinase inhibitor that binds tightly to LRRK2 with structural evidence that it stabilizes an open kinase conformation. We selected Ponatinib as our initial candidate inhibitor as it has a reported Ki for LRRK2 of 31 nM[34], and crystal structures show it bound to RIPK235 and IRAK4 in open conformations (Extended Data Fig. 14). We confirmed that Ponatinib also inhibited LRRK2^{RCKW} by monitoring phosphorylation of the known LRRK2 substrate, Rab8a8 *in vitro* (Extended Data Fig. 15a).

As our hypothesis predicted, Ponatinib rescued kinesin motility in a dose-dependent manner at concentrations of LRRK2^{RCKW} (25 nM) that had resulted in almost complete inhibition of the motors (Fig. 5a, Extended data Fig. 15b-e). We observed similar effects with GZD-824, a chemically-related Type 2 kinase inhibitor[36] (Fig. 5a and Extended Data Fig. 15d, e). Our hypothesis also predicted that kinase inhibitors that stabilize the closed form of the kinase should be unable to rescue the motors and may even enhance the inhibitory effect of LRRK2^{RCKW} by increasing its interaction with microtubules. Indeed, the LRRK2-specific Type 1 inhibitors MLi-2[37,38] and LRRK2-IN-1[39], which are known[40] or expected[37] to stabilize a closed conformation of the kinase, further enhanced the inhibitory activity of LRRK2^{RCKW} on kinesin motility (Fig. 5a). As was the case with Ponatinib, GZD-824, MLi-2 and LRRK2-IN-1 all inhibited phosphorylation of Rab8a by LRRK2^{RCKW} (Extended Data Fig. 15a). Similar to kinesin, dynein motility was rescued by Ponatinib and GZD-824, but not MLi-2 or LRRK2-IN-1 (Fig. 5b and Extended Data Fig. 15d, f). These data suggest that the effects of LRRK2 kinase inhibitors on microtubule-based motility should be taken into account when designing LRRK2-targeted PD therapeutics.

GZD-824 reduces filament formation in cells

In cells, LRRK2 forms filaments that colocalize with a subset of microtubules and are sensitive to the microtubule depolymerizing drug nocodazole13. This association is enhanced by the PD-linked mutations R1441C, R1441G, Y1699C and I2020T13,41 and by Type 1 kinase inhibitors[39,42]. We tested our kinase conformation hypothesis in 293T cells by determining if Type 1 and Type 2 kinase inhibitors had opposite effects on the formation of cellular microtubule-associated LRRK2 filaments. Consistent with previous findings, the Type 1 inhibitor MLi-2 enhanced LRRK2's-microtubule association (Fig. 5c, d), suggesting that the closed conformation of the kinase favors binding to microtubules in cells. In contrast, we found that the

Type 2 inhibitor GZD-824 reduced the filament-forming ability of overexpressed LRRK2 (carrying the mutation I2020T; Fig. 5e, f). This reduction in LRRK2 filament formation was not due to changes in LRRK2 protein expression levels (Extended Data Fig. 16a, b) or the overall architecture of the microtubule cytoskeleton (Extended Data Fig. 16c).

CONCLUSIONS

Here we reported the 3.5Å structure of the catalytic half of LRRK2 (LRRK2^{RCKW}), where most major PD-linked mutations are located. Our model represents the first structure of a large portion of human LRRK2 with sufficient resolution to yield molecular information about LRRK2's activity and its regulation. LRRK2^{RCKW} is J-shaped, which brings its GTPase (RoC domain) and kinase in close proximity despite their separation along the linear sequence of LRRK2. The direct contact we observe between the C-lobe of the kinase and COR-A, which is closely associated with the GTPase, provides a structural context for the cross-talk between these two catalytic domains (reviewed in[26]). Our cryo-EM structure, obtained in the absence of kinase inhibitors, shows the kinase in an open (inactive) conformation. A unique feature of the structure is a long alpha helix located at the C-terminus of LRRK2, following the WD40 domain. Running along the long axis of the kinase domain, this helix has multiple interactions with both its N- and C-lobes. Given these interactions, and the presence of a known phosphorylation site near its end (T2524)[31], it is likely that this helix plays an important role in regulating LRRK2's kinase activity.

Our ability to generate microtubule-associated LRRK2^{RCKW} filaments using purified components demonstrates that these filaments can form in the absence of other proteins and that the C-terminal half of LRRK2 is sufficient for their assembly. This is also in agreement with the observation that our LRRK2^{RCKW} structure accounts for the filament density observed in a recent 14Å structure of LRRK2-microtubule associated filaments in cells obtained by cryo-ET[21].

We used the high-resolution structure of LRRK2^{RCKW}, in combination with the 14Å *in situ* structure[21], to build an atomic model of the microtubule-associated LRRK2 filaments. Docking of our LRRK2^{RCKW} structure, with its open kinase domain, into the microtubule-associated *in situ* structure led to significant steric clashes. These clashes were largely resolved by modeling LRRK2's kinase in a closed conformation, leading us to hypothesize that the conformation of LRRK2's kinase controls its association with microtubules, with a closed conformation favoring its oligomerization on microtubules (Fig. 5g). In our model of microtubule-associated LRRK2^{RCKW} filaments, the filaments form through head-head and tail-tail interactions involving either the COR or WD40 domains of LRRK2. Formation of these interfaces does not require LRRK2 to interact with microtubules, as we obtained lower resolution cryo-EM structures of both types of LRRK2^{RCKW} dimers in the absence of microtubules. In addition, aligning atomic models of these dimers *in silico* resulted in a right-handed filament with similar geometric properties to the LRRK2 filaments observed in cells[21]. Thus, the ability of LRRK2 to form filaments is a property inherent to LRRK2, and specifically the RCKW domains. Since LRRK2^{RCKW} exists both as a monomer and dimer in solution, it remains to be determined what the minimal filament-forming unit is. We propose that the surface charge complementarity between the microtubule and LRRK2, as well as the size and shape of the microtubule stimulates the formation of LRRK2 filaments.

We tested the model that the conformation of LRRK2's kinase regulates microtubule association both *in vitro* and in cells using kinase inhibitors that are known or expected to stabilize either the open (Type 2) or closed (Type 1) kinase conformations. In support of our model, Type 2 inhibitors relieved the LRRK2^{RCKW}-dependent inhibition of the microtubule-based motors kinesin and dynein and reduced LRRK2 filament formation in cells, while Type 1 inhibitors failed to rescue the motors and enhanced filament formation in cells. In contrast to our structural studies, which used high concentrations of LRRK2^{RCKW} (cryo-EM) or overexpressed LRRK2 in cells (cryo-ET), our single-molecule motility assays showed that low nanomolar

concentrations of LRRK2^{RCKW} negatively impact the microtubule-based motility of both kinesin and dynein *in vitro*. At these low concentrations it is likely that LRRK2 would not form the long, highly ordered filaments and microtubule bundles observed in cells overexpressing the protein; instead, we hypothesize that at endogenous expression levels in cells LRRK2 forms short stretches of filaments on microtubules.

Our data showing that increasing concentrations of LRRK2^{RCKW} dramatically shorten the distance kinesin moves (run length), without affecting its velocity suggest that LRRK2 acts as a roadblock. Other microtubule-associated proteins (MAPs), such as MAP2 and Tau, also inhibit kinesin motors[43] (bioRxiv 10.1101/731604). In contrast to kinesin, dynein is largely unaffected by MAP2 and Tau[43] (bioRxiv 10.1101/731604), likely due to its ability to sidestep to adjacent protofilaments[44-46]. LRRK2's unusual ability to inhibit dynein motility may be a consequence of its forming oligomers that block dynein's sidestepping.

What is the physiological role of non-pathogenic microtubule-associated LRRK2? Our data show that low nanomolar concentrations of LRRK2 act as a roadblock for microtubule-based motors. Dynein and kinesin have been shown to bind directly or indirectly to many Rab-marked cargos[47-51]. Our data also show that the microtubule-associated form of LRRK2 has its kinase in a closed (and potentially active) conformation. Given this, it is possible that when microtubule-associated LRRK2 stalls the movement of kinesin and dynein, this increases the likelihood that LRRK2 will phosphorylate cargo-associated Rab GTPases on their switch 2 region[8], ultimately leading to effector dissociation[8] and cargo release. This scenario suggests that increased microtubule binding by LRRK2 carrying PD mutations could (1) block membrane transport driven by molecular motors by acting as a roadblock, (2) lead to increased phosphorylation of physiological microtubule-associated substrates and/or phosphorylation of non-physiological substrates, or (3) a combination of the first two points. In support of this idea, the four familial PD mutations that enhance LRRK2 microtubule binding[13] also show higher levels of Rab GTPase phosphorylation in cells than the G2019S LRRK2 mutant[8,9,52], whose

microtubule binding is not enhanced over wild-type LRRK2[13]. Testing this and other models is an important future direction to understand the cell biological function of both wild-type and pathogenic LRRK2.

Regardless of what role LRRK2's binding to microtubules plays in PD, our data have important implications for the design of LRRK2 kinase inhibitors for therapeutic purposes. Our data predict that treatment with inhibitors that promote binding of LRRK2 to microtubules by favoring a closed conformation of its kinase will block microtubule-based trafficking, while inhibitors that favor an open conformation of the kinase will not.

Chapter 1, in full, is a reprint of material as it appears in Parkinson's Disease-Linked LRRK2 Structure and Model for Microtubule Interaction, 2020. Colin K. Deniston, John Salogiannis, Sebastian Mathea, David M. Snead, Indarjit Lahiri, Oscar Donosa, Reika Watanabe, Jan Böhning, Andrew K. Shiau, Stefan Knapp, Elizabeth Villa, Samara L. Reck-Peterson, Andres E. Leschziner., Nature, 2020. The dissertation author was a co-author of this paper.

METHODS

Cloning, plasmid construction, and mutagenesis

For baculovirus expression, the DNA coding for the LRRK2 residues 1327 to 2527 (taken from Mammalian Gene Collection) was PCR-amplified using the forward primer TACTTCCAATCCATGAAAAAGGCTGTGCCTTATAACCGA and the reverse primer TATCCACCTTTACTGTCACTCAACAGATGTTCGTCTCATTTTTTCA. The T4 polymerase-treated amplicon was inserted into the expression vector pFB-6HZB by ligation-independent cloning. According to Bac-to-Bac expression system protocols (Invitrogen), this plasmid was used for the generation of recombinant Baculoviruses.

For mammalian expression vectors, pDEST53-GFP-LRRK2 (WT)[56] from Addgene (#25044) was used. pDEST53-GFP-LRRK2 (I2020T) was cloned using QuikChange site-directed mutagenesis (Agilent) with the forward primer AAGATTGCTGACTACGGCACTGCTCAGTACTGCTG and the reverse primer CAGCAGTACTGAGCAGTGCCGTAGTCAGCAATCTT. pET17b-Kif5b(1-560)-GFP-His[57] was obtained from Addgene (#15219). For pET28a-ZZ-TEV-Halo-NINL1-702, Ninein-like1-702 (NINL) was synthesized as previously described[33] and inserted into a pET28a expression vector with a synthesized ZZ-TEV-Halo gBlock fragment (IDT) using Gibson assembly.

LRRK2^{RCKW} expression and purification

The expression construct contained an N-terminal His6-Z-tag, cleavable with TEV protease (Extended Data Fig. 1). For LRRK2^{RCKW} purification, the pelleted Sf9 cells were washed with PBS, resuspended in lysis buffer (50 mM HEPES pH 7.4, 500 mM NaCl, 20 mM imidazole, 0.5 mM TCEP, 5% glycerol, 5 mM $MgCl_2$, 20 µM GDP) and lysed by sonication. The lysate was cleared by centrifugation and loaded onto a Ni-NTA (Qiagen) column. After vigorous rinsing with lysis buffer the His6-Z tagged protein was eluted in lysis buffer containing 300 mM imidazole. Immediately thereafter, the eluate was diluted with a buffer containing no NaCl, in order to reduce the NaCl-concentration to 250 mM and loaded onto an SP sepharose column. His6-Z-TEV-LRRK2^{RCKW} was eluted with a 250 mM to 2.5 M NaCl gradient and treated with TEV protease overnight to cleave the His6-Z-tag. Contaminating proteins, the cleaved tag, uncleaved protein and TEV protease were removed by another combined SP sepharose Ni-NTA step. Finally, LRRK2^{RCKW} was concentrated and subjected to gel filtration in storage buffer (20 mM HEPES pH 7.4, 800 mM NaCl, 0.5 mM TCEP, 5% glycerol, 2.5 mM $MgCl_2$, 20 µM GDP) using

an AKTA Xpress system combined with an S200 gel filtration column. The final yield as calculated from UV absorbance was 1.2 mg $LRRK2^{RCKW}$/L insect cell medium.

SEC-MALS

SEC-MALS experiments were performed using an ÄKTAmicro chromatography system hooked up to a Superdex 200 Increase 3.2/300 size exclusion chromatography column coupled in-line to a DAWN HELEOS II multiangle light scattering detector (Wyatt Technology) and an Optilab T-rEX refractive index detector (Wyatt Technology). SEC-MALS was performed in 50 mM Hepes pH 7.4, 200 mM NaCl 0.5 mM TCEP, 5% glycerol, 5 mM $MgCl_2$, and 20 μM GDP. For a typical sample, 50 uL of ~7 μM $LRRK2^{RCKW}$ was injected onto the column. Molar mass was calculated using ASTRA 6 software, with protein concentration derived from the Optilab T-rEX. $LRRK2^{RCKW}$ used for SEC-MALS experiments contained an extra 16 residue N-terminal Gly-Ser linker sequence.

Electron microscopy

Electron microscopy sample preparation and imaging of trimer dataset

Purified $LRRK2^{RCKW}$ was dialyzed into a final buffer consisting of 20mM HEPES pH7.4, 80mM NaCl, 0.5mM TCEP, 5% glycerol, 2.5mM $MgCl_2$ and 20μM GDP and then diluted to a final concentration of 4μM in the same buffer. This sample was applied to glow-discharged (20mA for 20s in a K100 Instrument) UltrAuFoil Holey Gold R 1.2/1.3 grids (Quantifoil). A Vitrobot (FEI) was then used to blot away excess sample and plunge freeze the grids in liquid ethane. Grids were stored in liquid nitrogen until imaged.

Cryo-EM data was collected at UCLA California NanoSystems Institute in a Titan Krios (FEI) operated at 300kV, equipped with a K2 Summit direct electron detector (Gatan) and a Quantum energy filter (Gatan). Automated data collection was performed using Leginon[58]. We recorded a total of 3,824 movies in 'counting mode' at a dose rate of 6.65 electrons Å-2 sec-1 with a total exposure time of 8s sub-divided into 200ms frames, for a total of 40 frames. The images were recorded at a nominal magnification of 130,000x resulting in an object pixel size of 1.07Å. The defocus range of the data was -1µm to -1.8µm.

Electron microscopy map and model generation of trimer dataset

We aligned the movie frames using UCSF MotionCor2[59], using the dose-weighted frame alignment option. We estimated the CTF on dose-weighted images using GCTF version 1.0660 as implemented in Appion[61] with per-particle CTF generation. Images having CTF fits worse that 5Å (as determined by GCTF) were excluded from further processing. Using this approach, 3,693 micrographs were kept for further processing. We selected particles from micrographs using FindEM[62] with projections of a trimeric $LRRK2^{RCKW}$ map, created from an initial Cryosparc *ab initio* model generation, serving as a reference. Particle picking was performed within the framework of Appion, resulting in a data set of 836,956 particles.

We carried out subsequent processing first in Relion 3.0[63] then in CryoSparc2[64]. A series of 2D and 3D classifications were performed as shown in Extended Data Fig. 2c to generate the final map. The initial reference was created in a similar manner to those used for template picking, from an initial *ab initio* model generated in Cryosparc. All references were filtered to either 60Å (default in Relion) or 30Å (default in CryoSparc) before refinement processes. The final map, generated in Cryosparc2 using non-uniform refinement and while applying C3 symmetry, reached 3.47Å resolution. Initial 2D classifications used binned data (4.28Å $pixel^{-1}$)

while all subsequent 3D classifications and refinement steps used unbinned images (1.07Å pixel^{-1}).

In order to improve the density corresponding to the RoC and COR-A domains, a second map was generated following a different processing scheme, which used signal subtraction and is shown in Extended Data Fig. 2f. The final refinement led to a 3.8Å map of LRRK2^{RCKW}. All the steps used unbinned images (1.07Å pixel^{-1}).

The resolutions of the cryo-EM maps, here and below, were estimated from Fourier Shell Correlation (FSC) curves calculated using the gold-standard procedure and the resolutions are reported according to the 0.143 cutoff criterion[65,66]. FSC curves were corrected for the convolution effects of a soft mask applied to the half maps by high-resolution phase randomization[67]. For display and analysis purposes, we sharpened the maps with automatically estimated negative B factors from Relion[63] or CryoSparc2[64].

We built the LRRK2^{RCKW} models using both the 3.47Å C3 and 3.8Å density-subtracted maps. We used a combination of Rosetta[22] and manual building in Coot[68] to build all models. Starting models were found via a sequence alignment search in HHpred[69] and the top 5 results for each domain were used in the initial fitting of the backbone. We built the COR-B, KIN, and WD40 domains using the density of the 3.47Å C3 map and the RoC and COR-A domains using the 3.8Å map, then connected the two after fitting them into the 3.8Å map. Finally, we performed multiple iterations of both the CM and Relax functions in Rosetta, along with manual manipulation in Coot, to build our final 20 models (10 including GDP-Mg^{2+} in the RoC domain, and 10 excluding it). In areas of weak density, we either removed part of the polypeptide chain or, where only side chain density was poor, converted the chain to poly-alanine.

The GDP-Mg^{2+} was placed in our model by initially aligning a structure of the RoC domain containing a bound GDP-Mg^{2+} (PDB: 2zej)[17] to the RoC domain in our structure. The GDP-Mg^{2+} was then added to our model in the aligned position and run through Rosetta to allow for fine movements into our density and re-arrangement of nearby chains.

The phosphorylation of the threonine residue 1343, which we observe in our map and is a known phosphorylation site of Roco family GTPases[70], was confirmed by phosphor-enrichment mass spec (data not shown).

Electron microscopy sample preparation, imaging, and processing of apo, MLi2, Ponatinib LRRK2^{RCKW} monomer/dimers

For all samples, purified LRRK2^{RCKW} was dialyzed into the same final buffer as described for the trimer data, then diluted to its final concentration in the same buffer. Unlike with the trimer data, however, the following datasets were collected from multiple grids prepared using slightly different sample conditions and imaged using a range of microscope settings.

The apo LRRK2^{RCKW} monomer dataset had sample diluted to final concentrations ranging between 1μM and 6μM. In addition, one dataset was collected with the grid tilted to 30^{o} to overcome preferred orientation issues. Otherwise, grids were prepared as described for the trimer dataset.

The apo LRRK2^{RCKW} dimer dataset had sample diluted to final concentrations ranging between 4μM and 12μM. Two of the samples contained 0.05mM Digitonin (Sigma, D141) or 0.03% octyl glucoside (Sigma, O8001) detergents to overcome preferred orientation issues. One dataset was collected with the grid tilted to 30^{o}, also to overcome preferred orientation issues. Otherwise, grids were prepared as described for the trimer dataset.

The MLi-2 LRRK2^{RCKW} dimer dataset had sample diluted to final concentrations of either 3μM or 4μM. MLi-2 was added post-dialysis to a final concentration of 5μM. The sample was incubated on ice for at least one hour before being applied to the grid. Otherwise, grids were prepared as described for the trimer dataset.

The ponatinib LRRK2^{RCKW} dimer dataset had sample diluted to final concentrations of 2μM or 4μM. Ponatinib was added post-dialysis at a concentration of either 5μM or 100μM. The

sample was incubated on ice for at least one hour before being applied to the grid. Otherwise, grids were prepared as described for the trimer dataset.

The apo LRRK2^{RCKW} monomer cryo-EM data was collected on a Talos Arctica (FEI) operated at 200kV, equipped with a K2 Summit direct electron detector (Gatan). Automated data collection was performed using Leginon[58]. A total of 11,354 movies were collected. We imaged samples at dose rates between 4.2 and 10 electrons Å^{-2} sec^{-1} with total exposure times ranging from 6s to 12s sub-divided into 200ms frames, for a total of 30 or 60 frames. All the images were recorded at nominal magnification of 36,000x (either counting or super resolution mode) resulting in object pixel sizes of either 1.16Å or 0.58Å, respectively. The defocus range of the data was -1µm to -2µm.

Frame alignment, CTF estimation and image selection were performed as described for the trimer dataset except that per-particle CTF was not used, instead the CTF information of the whole image was used. After selection we had 7,067 micrographs. Particles were extracted using crYOLO[71]. We carried out subsequent processing in CryoSparc2[64] on binned images (2.32Å pixel^{-1}).

A series of 2D and 3D classifications were performed as shown in Extended Data Fig. 8 to generate the final map. The initial monomer reference, used for refinement of the monomer map, was generated from our LRRK2^{RCKW} model. The initial dimer references, used for particle sorting, were generated as shown in Extended Data Fig. 7. All references were filtered to 30Å, the default value in CrypSparc2, before refinement processes. This final map reached a resolution of 8.08Å using non-uniform refinement.

The apo LRRK2^{RCKW} dimer cryo-EM data was collected as described for the apo LRRK2^{RCKW} monomer. A total of 5,303 movies were collected. We imaged samples at dose rates between 4.6 and 7.8 electrons Å^{-2} sec^{-1} with total exposure times ranging between 7s and 11s sub-divided into 200ms frames, for a total of 35 or 55 frames. All the images were recorded at nominal magnification of 36,000x (either counting mode or super resolution mode) resulting in

object pixel sizes of either 1.16Å or 0.58Å, respectively. The defocus range of the data was -1µm to -2µm.

Frame alignment, CTF estimation, image selection, and particle picking were performed as described for the apo LRRK2^{RCKW} monomer. After selection we had 3,100 micrographs. We carried out subsequent processing in CryoSparc2[64] on binned images (2.32Å pixel^{-1}).

The classification and refinement scheme for the apo LRRK2^{RCKW} WD40- and COR-mediated dimer maps is shown in Extended Data Fig. 8. The same initial dimer references used for the apo LRRK2^{RCKW} monomer, filtered to the same resolution, were used here for refinement of the dimer maps. In addition, a linear trimer reference, generated from stitching together the two initial dimer references and filtered to the same resolution, was used during the initial 3D classification step to sort out oligomers longer than two subunits which harm downstream alignment. The final maps had resolutions of 13.39Å (WD40-mediated dimer) and 9.52Å (COR-mediated dimer) with C2 symmetry applied to both.

The MLi-2 LRRK2^{RCKW} dimer cryo-EM data was collected as described for the apo LRRK2^{RCKW} monomer. We recorded a total of 4,139 movies. We imaged all datasets at a dose rate of 5.5 electrons Å^{-2} sec^{-1}, with total exposure times of either 9s or 10s sub-divided into 200ms frames, for a total of 45 or 50 frames. All the images were recorded at a nominal magnification of 36,000x (counting mode) resulting in object pixel sizes of 1.16Å. The defocus range of the data was -1µm to -2µm.

Frame alignment, CTF estimation, image selection, and particle picking were performed as described for the apo LRRK2^{RCKW} monomer. After selection, 4,030 micrographs were kept for further processing. Processing was done in Relion 3.0[63] then CryoSparc2[64] using binned images (2.32Å pixel^{-1}).

The classification and refinement scheme for the MLi-2 LRRK2^{RCKW} WD40- and COR-mediated dimer maps is shown in Extended Data Fig. 9. The same references used for the apo LRRK2^{RCKW} dimers, and filtered to the same resolution, were used here for the same purposes.

The final maps had resolutions of 9.74Å (WD40-mediated dimer) and 9.04Å (COR-mediated dimer), with no symmetry applied.

The Ponatinib LRRK2^{RCKW} dimer cryo-EM data was collected as described for the apo LRRK2^{RCKW} monomer. We recorded a total of 1,797 movies. We imaged all dose rates of either 5.5 or 9.7 electrons Å^{-2} sec^{-1} with total exposure times of 7s or 10s sub-divided into 200ms frames, for a total of 35 or 50 frames. All the images were recorded at a nominal magnification of 36,000x (counting mode) resulting in object pixel sizes of 1.16Å. The defocus range of the data was -1µm to -2µm.

Frame alignment, CTF estimation, image selection, and particle picking were performed as described for the apo LRRK2^{RCKW} monomer. 1,455 micrographs were kept for further processing. Processing was done in CryoSparc2[64] on binned images (2.32Å pixel^{-1}). Ponatinib LRRK2^{RCKW} dimer particles were sorted via 3D and 2D classification leading to the final 2D averages shown in Extended Data Fig. 10.

Electron microscopy sample preparation and imaging of microtubule-bound LRRK2^{RCKW}

Purified LRRK2^{RCKW} was dialyzed into the same buffer used for the trimer dataset with the addition of 20µM Taxol and then diluted to a final concentration of 3µM in the same buffer. Microtubules, made as previously described[57], were then added to a final concentration of 3µM (tubulin dimer concentration). The mixture was incubated at room temperature for a minimum of 5 minutes before being applied to the grid. Grids were prepared as described for the trimer dataset except that Quantifoil C-flat 1.2/1.3 carbon open hole grids were used.

Cryo-EM data was collected on a Talos Arctica (FEI) operated at 200kV, equipped with a K2 Summit direct electron detector (Gatan) using Leginon[58]. We recorded a total of 10 movies. We imaged at a dose rate of 7.9 electrons Å^{-2} sec^{-1} with a total exposure time of 7s sub-divided into 200ms frames, for a total of 45 frames. All the images were recorded at a nominal

magnification of 36,000x (super resolution mode) resulting in object pixel sizes of 0.58Å. The defocus range of the data was -1µm to -2µm. Images were aligned using MotionCor2[59].

Building the molecular model of microtubule-associated LRRK2^{RCKW} filaments

Given that the WD40 densities are clearly identifiable in the sub-tomogram average of microtubule (MT)-associated LRRK2, we used these as a starting point for docking the structure of LRRK2^{RCKW} into the cryo-ET map. First, a synthetic dimer of the WD40 domains from the LRRK2^{RCKW} structure was generated by aligning them to a crystal structure of the isolated WD40 domain, which formed a dimer in the crystal (PDB: 6DLP)[18]. This synthetic dimer was then docked into the sub-tomogram average in Chimera, using the Fit in Map function with the options of filtering the structure to the resolution of the map (14Å) and optimizing correlation. A WD40 dimer was placed into each of the two corresponding densities present in the map. Then, four copies of the LRRK2^{RCKW} structure were added by aligning their WD40 domains to those previously docked into the sub-tomogram average. The same procedure was followed to build the filament using the "closed" kinase model of LRRK2^{RCKW} (see section below for how that model was generated).

Backbone clashes at the COR-mediated interface in the model filament were measured in Chimera (with default settings) after converting the four LRRK2^{RCKW} monomers to poly-alanine models.

Modeling a "closed" kinase version of LRRK2^{RCKW}

In order to identify a good reference to model the closed state of LRRK2^{RCKW}'s kinase, we ran separate structural searches (using the DALI server) with the N- and C-lobes of LRRK2^{RCKW}'s kinase domain. We looked through the matches for a kinase that scored highly

with both lobes, and whose structure is in a closed state. We selected Interleukin-2 inducible T-cell kinase (Itk) bound to an inhibitor as our reference (PDB: 3QGY)[54].

LRRK2^{RCKW} was split at the junction between the N- and C-lobes of its kinase domain (L1949-A1950), resulting in one half containing the RoC, COR, and kinase (N-lobe) domains and another containing the kinase (C-lobe) and WD40 domains. The C-lobe of 3QGY was then aligned (in Chimera) to the C-lobe of LRRK2^{RCKW}'s kinase domain, and subsequently the N-lobe of LRRK2^{RCKW}'s kinase was aligned to the N-lobe of 3QGY. The two halves were then combined to generate the "closed" kinase model of LRRK2^{RCKW}.

Docking of LRRK2^{RCKW} into cryo-EM maps of monomers and dimers

In order to build models of WD40- and COR-mediated dimers of LRRK2^{RCKW} in the presence of MLi-2, we again split LRRK2^{RCKW} at the junction between the N- and C-lobes (L1949-A1950). The two halves were fitted into one half of the cryo-EM map of a WD40-mediated dimer of LRRK2^{RCKW} obtained in the presence of MLi-2 (we chose this map as its resolution was higher than that of the COR-mediated dimer). We also docked the two halves of LRRK2^{RCKW} into a cryo-EM map of a LRRK2^{RCKW} monomer obtained in the absence of inhibitor. The fitting was done in Chimera using the Fit in Map function with the options of filtering the structure to the resolution of the map and optimizing correlation. The two halves were then joined to generate a full model of LRRK2^{RCKW}.

The WD40- and COR-mediated dimers of LRRK2^{RCKW} in the presence of MLi-2 were built by docking the models built above into the corresponding cryo-EM maps, using the same approach in Chimera as outlined above.

The LRRK2^{RCKW} "filament" shown in Extended Data Fig. 11 was generated by aligning, in alternating order, multiple copies of the two dimer models (WD40- and COR-mediated) built into the cryo-EM maps obtained in the presence of MLi-2.

Kinase inhibitors

Stocks of the kinase inhibitors MLi-2 (10 mM; Tocris), Ponatinib (10 mM; ApexBio), GZD-824 (10 mM; Cayman Chemical), and LRRK2-IN-1 (2 mM; Michael J Fox Foundation) were stored in DMSO at -20 C.

Antibodies

All antibodies used for immunocytochemistry were diluted to 1:500. Primary antibodies used were chicken anti-GFP (Aves Labs) and rabbit anti-alpha-tubulin (ProteichTech). Secondary antibodies used were goat anti-chicken-Alexa 488 (ThermoFisher) and goat anti-chicken Alexa568 (ThermoFisher). DAPI was used at 1:5000 according to the manufacturers suggestions (ThermoFisher). Primary antibodies used for Western blots were mouse anti-GFP (Santa Cruz, 1:1000 dilution) mouse anti-GAPDH (ProteinTech, 1:5000 dilution) and mouse anti-gamma-tubulin (ProteinTech, 1:5000 dilution). Secondary antibodies (1:15,000) used for Western blots were IRDye goat anti-mouse 680RD and IRDye goat anti-rabbit 780RD (Li-COR).

Rab8a expression and purification

N-terminally tagged (His6-ZZ) Rab8a containing a TEV cleavage site was cloned into a PET28a expression vector and expressed in BL21(DE3) E. coli cells. Transformed cells were grown overnight at 37ºC in 10 mL LB medium containing kanamycin (50 µg/ml), then diluted into 200 mL LB medium containing kanamycin (50 µg/ml), grown to an optical density at 600 nm of ~1-2, diluted into 4 L LB medium containing kanamycin (50 µg/ml), and grown to an optical density at 600 nm of 0.4. IPTG was added (final concentration 0.5 mM) to induce protein

expression for ~18 hours at 18ºC. Cells were harvested by centrifugation at 8983 x g for 10 min at 4ºC, followed by resuspension in 15 mL LB medium and centrifugation at 2862 x g for 10 min at 4ºC. The cell pellet was flash frozen in liquid nitrogen and stored at -80ºC. For a typical protein purification, cell pellets were resuspended in lysis buffer (50 mM HEPES pH 7.4, 200 mM NaCl, 2 mM DTT, 10% glycerol, 5 mM $MgCl_2$, 0.5 mM Pefabloc, and protease inhibitor cocktail tablets) and lysed by sonication on ice. The lysate was clarified by centrifugation at 164,700 x g for 40 mins at 4ºC and then incubated with Ni-NTA agarose beads (Qiagen) for 1 hour at 4ºC. Beads were extensively washed with wash buffer (50 mM HEPES pH 7.4, 150 mM NaCl, 2 mM DTT, 10% glycerol, 5 mM $MgCl_2$); His6-ZZ-Rab8a was eluted in 40 mL elution buffer (50 mM HEPES pH 7.4, 150 mM NaCl, 300 mM imidazole, 2 mM DTT, 10% glycerol, 5 mM $MgCl_2$). The protein eluate was diluted 2 fold in wash buffer, incubated with IgG sepharose 6 fast flow beads equilibrated in wash buffer, incubated at 4ºC for 2.5 hours, and washed extensively in wash buffer. Protein-bound IgG beads were then transferred into TEV buffer (50 mM HEPES pH 7.4, 200 mM NaCl, 2 mM DTT, 10% glycerol, 5 mM $MgCl_2$), and untagged Rab8a was cleaved off of IgG sepharose beads by incubation with TEV protease at 4ºC overnight. The next day, cleaved Rab8a was separated from His6-TEV protease and any remaining uncleaved protein or residual tag by incubation with Ni-NTA agarose beads (Qiagen), followed by washing with TEV buffer containing 25 mM imidazole. Lastly, purified Rab8a was run over a Superdex 200 increase 10/300 size exclusion column equilibrated in S200 buffer (50 mM HEPES pH 7.4, 200 mM NaCl, 2 mM DTT, 1% glycerol, 5 mM $MgCl_2$), and concentrated and exchanged into buffer containing 10% glycerol for storage at -80ºC.

In vitro phosphorylation of Rab8a by $LRRK2^{RCKW}$

Purified Rab8a (~3.8 µM) was phosphorylated by $LRRK2^{RCKW}$ (~38 nM) in a buffer containing 50 mM HEPES pH 7.4, 80 mM NaCl, 10 mM $MgCl_2$, 0.5 mM TCEP, 1 mM ATP, 200

μM GDP); 34 μL reaction mixtures containing kinase inhibitor or an equivalent volume DMSO were incubated at 30ºC, and samples were taken at 45 mins, and 90 mins. An effective reaction volume of 0.75 μL was run on a 4-12% Bis-Tris protein gel, transferred to nitrocellulose, and blotted with a commercially available antibody to pT72-Rab8a (MJFF-pRab8) as previously described[72] and per manufacturer's instructions, with the exception that HRP-labeled secondary antibody was used at a dilution of 1:2000.

Purification of molecular motors

Protein purification steps were done at 4°C unless otherwise indicated. Human KIF5B1-560 (K560)-GFP was purified from E. coli using an adapted protocol previously described[73]. pET17b-Kif5b(1-560)-GFP-His was transformed into BL-21[DE3] RIPL cells (New England Biolabs) until OD 0.6-0.8 and expression was induced with 0.5 mM IPTG for 16 hr at 18°C. Frozen pellets from 2 L culture were resuspended in 40 mL lysis buffer (50 mM Tris, 300 mM NaCl, 5 mM $MgCl_2$, and 0.2 M sucrose, pH 7.5) supplemented with 1 cOmplete EDTA-free protease inhibitor cocktail tablet (Roche) per 50 mL and 1 mg/mL lysozyme. The resuspension was incubated on ice for 30 min and lysed by sonication. Sonicate was supplied with 10 mM imidazole and 0.5 mM PMSF and clarified by centrifuging at 30,000 x g for 30 min in Type 70 Ti rotor (Beckman). The clarified supernatant was incubated with 5 mL Ni-NTA agarose (Qiagen) and rotated in a nutator for 1 hr. The mixture was washed with 30 mL wash buffer (50 mM Tris, 300 mM NaCl, 5 mM $MgCl_2$, 0.2 M sucrose, and 20 mM imidazole, pH 7.5.) by gravity flow. Beads were resuspended in elution buffer (50 mM Tris, 300 mM NaCl, 5 mM $MgCl_2$, 0.2 M sucrose, and 250 mM imidazole, pH 8.0), incubated for 5 mins, and eluted stepwise in 0.5 mL increments. Peak fractions were combined and buffer exchanged on a PD-10 desalting column (GE Healthcare) equilibrated with storage buffer (80 mM PIPES, 2 mM $MgCl_2$, 1 mM EGTA, and 0.2 M sucrose, pH 7.0). From this, peak fractions of motor solution were either flash frozen at -

80°C until further use or immediately subjected to microtubule bind and release purification. A total of 1 mL motor solution was incubated with 1 mM AMP-PNP and 20 μM taxol on ice for 5 mins and warmed to room temperature (RT). For microtubule bind and release, polymerized bovine brain tubulin was centrifuged through a glycerol cushion (80 mM PIPES, 2 mM $MgCl_2$, 1 mM EGTA, and 60 % glycerol (v/v) with 20 μM taxol and 1 mM DTT) and resuspended as previously described[32] was incubated with motor solution in the dark for 15 mins at RT. The Motor-microtubule mixture was laid on top of a glycerol centrifuged in a TLA120.2 rotor at 278,835 x g for 12 min at RT. Final pellet (Kinesin-bound microtubules) was washed with BRB80 (80 mM PIPES, 2 mM $MgCl_2$, and 1 mM EGTA, pH 7.0) and incubated in 100 μL of release buffer (80 mM PIPES, 2 mM $MgCl_2$, 1 mM EGTA, and 300 mM KCl, pH ~7 with 5mM Mg-ATP) for 5 mins at RT. The supernatant was supplied with 660 mM sucrose and flash frozen. A typical kinesin prep yielded ~0.5 to 1 μM K560-GFP dimer.

Human dynactin was purified from stable cell lines expressing p62-Halo-3xFlag as described previously[74]. Briefly, cells were collected from 160 x 15 cm plates and resuspended in 80 mL of dynactin-lysis buffer (30 mM HEPES [pH 7.4], 50 mM potassium acetate, 2 mM magnesium acetate, 1 mM EGTA, 1 mM DTT, 10% (v/v) glycerol) supplemented with 0.5 mM Mg-ATP, 0.2% Triton X-100 and 1 cOmplete EDTA-free protease inhibitor cocktail tablet (Roche) per 50 mL and rotated slowly for 15 min. The lysate was clarified by centrifuging at 66,000 x g for 30 min in Type 70 Ti rotor (Beckman). The clarified supernatant was incubated with 1.5 mL of anti-Flag M2 affinity gel (Sigma-Aldrich) overnight on a roller. The beads were transferred to a gravity flow column, washed with 50 mL of wash buffer (dynactin-lysis buffer supplemented with 0.1 mM Mg-ATP, 0.5 mM Pefabloc and 0.02% Triton X-100), 100 mL of wash buffer supplemented with 250 mM potassium acetate, and again with 100 mL of wash buffer. Dynactin was eluted from beads with 1 mL of elution buffer (wash buffer with 2 mg/mL of 3xFlag peptide). The eluate was collected, filtered by centrifuging with Ultrafree-MC VV filter (EMD Millipore) in a tabletop centrifuge and diluted to 2 mL in Buffer A (50 mM Tris-HCl [pH

8.0], 2 mM MgOAc, 1 mM EGTA, and 1 mM DTT) and injected onto a MonoQ 5/50 GL column (GE Healthcare and Life Sciences) at 1 mL/min. The column was pre-washed with 10 column volumes (CV) of Buffer A, 10 CV of Buffer B (50 mM Tris-HCl [pH 8.0], 2 mM MgOAc, 1 mM EGTA, 1 mM DTT, 1 M KOAc) and again with 10 CV of Buffer A at 1 mL/min. To elute, a linear gradient was run over 26 CV from 35-100% Buffer B. Pure dynactin complex eluted from ~75-80% Buffer B. Peak fractions containing pure dynactin complex were pooled, buffer exchanged into a GF150 buffer supplemented with 10% glycerol, concentrated to 0.02-0.1 mg/mL using a 100K MWCO concentrator (EMD Millipore) and flash frozen in liquid nitrogen. Typical dynactin prep yields are between 150-300 nM.

Human dynein was purified from stable cells lines expressing an IC2-SNAPf-3xFlag as described previously[33]. Frozen pellets collected from ~60-100 x 15 cm plates were resuspended in dynein lysis buffer (25 mM HEPES pH 7.4, 50 mM KOAc, 2 mM MgOAc,1 mM EGTA, 10% glycerol (v/v), and 1 mM DTT) supplemented with 0.2% Triton X-100, 0.5 mM Mg-ATP, and cOmplete EDTA-free protease inhibitor cocktail. The lysate was centrifuged at 66,000 x g in a Ti-70 rotor for 30 mins. The clarified supernatant was incubated with 1 mL of anti-Flag M2 affinity gel (Sigma-Aldrich) overnight on a roller. Beads were collected by gravity flow and washed with 50 mL wash buffer (dynein lysis buffer with 0.02% Triton X-100 and 0.5 mM Mg-ATP) supplemented with protease inhibitors (cOmplete Protease Inhibitor Cocktail, Roche). Beads were then washed with 50 mL high salt wash buffer (25 mM HEPES, pH 7.4, 300 mM KOAc, 2 mM MgOAc, 10% glycerol, 1 mM DTT, 0.02% Triton X-100, 0.5 mM Mg-ATP), and then with 100 mL wash buffer. For labeling, beads were resuspended in 1 mL wash buffer and incubated with 5 μM SNAP-Cell TMR Star (New England BioLabs) for 10 min on the column at RT. Unbound dye was removed with 100 mL wash buffer at 4°C. Dynein was eluted with 1 mL of elution buffer (wash buffer containing 2 mg/mL 3xFLAG peptide). The eluate was collected, diluted to 2 mL in Buffer A (50 mM Tris pH 8.0, 2 mM MgOAc, 1 mM EGTA, and 1 mM DTT) and injected onto a MonoQ 5/50 GL column (GE Healthcare Life Sciences) at 0.5 mL/min. The

column was washed with 20 CV of Buffer A at 1 mL/min. To elute, a linear gradient was run over 40 CV into Buffer B (50 mM Tris pH 8.0, 2 mM MgOAc, 1 mM EGTA, 1 mM DTT, 1 M KOAc). Pure dynein complex elutes from ~60–70% Buffer B. Peak fractions were pooled and concentrated, 0.1 mM Mg-ATP and 10% glycerol were added and the samples were snap frozen in liquid nitrogen. A typical preparation yielded 150-300 nM dynein.

Human NINL was purified as previously described[74]. pET28a-ZZ-TEV-Halo-NINL1-702 was transformed into BL-21[DE3] cells (New England Biolabs) until OD 0.4-0.6 and expression was induced with 0.1 mM IPTG for 16 hr at 18°C. Frozen cell pellets from 1 L culture were resuspended in 40 mL of activator-lysis buffer (30 mM HEPES [pH 7.4], 50 mM potassium acetate, 2 mM magnesium acetate, 1 mM EGTA, 1 mM DTT, 0.5 mM Pefabloc, 10% (v/v) glycerol) supplemented with 1 cOmplete EDTA-free protease inhibitor cocktail tablet (Roche) per 50 mL and 1 mg/mL lysozyme. The resuspension was incubated on ice for 30 min and lysed by sonication. The lysate was clarified by centrifuging at 66,000 x g for 30 min in Type 70 Ti rotor (Beckman). The clarified supernatant was incubated with 2 mL of packed IgG Sepharose 6 Fast Flow beads (GE Healthcare Life Sciences) for 2 hr on a roller. The beads were transferred to a gravity flow column, washed with 100 mL of activator-lysis buffer supplemented with 150 mM potassium acetate and 50 mL of cleavage buffer (50 mM Tris–HCl [pH 8.0], 150 mM potassium acetate, 2 mM magnesium acetate, 1 mM EGTA, 1 mM DTT, 0.5 mM Pefabloc, 10% (v/v) glycerol). The beads were then resuspended and incubated in 15 mL of cleavage buffer supplemented with 0.2 mg/mL TEV protease overnight on a roller. The supernatant containing cleaved proteins were concentrated using a 50K MWCO concentrator (EMD Millipore) to 1 mL, filtered by centrifuging with Ultrafree-MC VV filter (EMD Millipore) in a tabletop centrifuge, diluted to 2 mL in Buffer A (30 mM HEPES [pH 7.4], 50 mM potassium acetate, 2 mM magnesium acetate, 1 mM EGTA, 10% (v/v) glycerol and 1 mM DTT) and injected onto a MonoQ 5/50 GL column (GE Healthcare and Life Sciences) at 0.5 mL/min. The column was pre-washed with 10 CV of Buffer A, 10 CV of Buffer B (30 mM HEPES [pH 7.4], 1 M potassium

acetate, 2 mM magnesium acetate, 1 mM EGTA, 10% (v/v) glycerol and 1 mM DTT) and again with 10 CV of Buffer A at 1 mL/min. To elute, a linear gradient was run over 26 CV from 0-100% Buffer B. The peak fractions containing unlabeled Halo-tagged NINL were collected and concentrated to using a 50K MWCO concentrator (EMD Millipore) to 0.2 mL. A typical NINL prep yield was ~5-10 μM dimer.

Single-molecule microscopy and motility assays

Single-molecule imaging was performed using total internal reflection fluorescence (TIRF) microscopy with an inverted microscope (Nikon, Ti-E Eclipse) equipped with a 100x 1.49 N.A. oil immersion objective (Nikon, Plano Apo), and a MLC400B laser launch (Agilent), with 405 nm, 488 nm, 561 nm and 640 nm laser lines. Excitation and emission paths were filtered using single bandpass filter cubes (Chroma), and emitted signals were detected with an electron multiplying CCD camera (Andor Technology, iXon Ultra 888). Illumination and image acquisition were controlled with NIS Elements Advanced Research software (Nikon), and the xy position of the stage was controlled with a ProScan linear motor stage controller (Prior).

Single-molecule motility were performed in flow chambers as previously described[33] using the setup shown in the schematic in Fig. 4A. Biotin-PEG-functionalized coverslips (Microsurfaces) were adhered to a Superfrost Plus Microscope slide (ThermoFisher) using double-sided scotch tape. Each slide contained four flow-chambers. Taxol-stabilized microtubules (~15mg/mL) with ~10% biotin-tubulin and ~10% Alex405-tubulin were prepared as described previously[33]. For each motility experiment, 1 mg/mL Strepdavidin (in 30 mM HEPES, 2 mM MgOAc, 1mM EGTA, 10% glycerol) was incubated in the flow chamber for 3 mins. A 1:150 dilution of taxol-stabilized microtubules in motility assay buffer (30 mM HEPES, 50 mM KOAc, 2 mM MgOAc, 1mM EGTA, 10% glycerol, 1 mM DTT, and 20 μM Taxol, pH 7.4) was added to the flow chamber for 3 mins to adhere polymerized microtubules to the coverslip. Flow

chambers containing adhered microtubules were washed twice with LRRK2 buffer (20 mM HEPES pH 7.4, 800 mM NaCl, 0.5 mM TCEP, 5% glycerol, 2.5 mM $MgCl_2$, 20 μM GDP). Flow chambers were then incubated for 5 mins either with (1) LRRK2 buffer alone or with the indicated kinase inhibitors ("0 nM" $LRRK2^{RCKW}$ condition) or (2) LRRK2 buffer containing $LRRK2^{RCKW}$ either alone, with DMSO, or with kinase inhibitors. DMSO or drugs were incubated with LRRK2 buffer (± $LRRK2^{RCKW}$) for 10 mins at RT before adding to the flow chambers. Prior to the addition of dynein and kinesin motors, the flow chambers were washed twice with motility assay buffer containing 1mg/mL casein. To assemble dynein-dynactin-ninein-like (NINL) complexes, purified dynein (10-15 nM), dynactin and NINL were mixed at 1:2:10 molar ratio and incubated on ice for 10 min. The final imaging buffer for motors contained motility assay buffer supplemented with an oxygen scavenger system, 71.5 mM β-mercaptoethanol and either 1 mM ATP (kinesin) or 2.5 mM ATP (dynein). The final concentrations of kinesin and dynein in the flow chambers were ~2.5 nM and ~0.3 nM, respectively. K560-GFP was imaged every 500 msecs for 2 mins with 25% laser (488) power at 150 ms exposure time. Dynein-TMR-dynactin-NINL was imaged every 300 msec for 3 mins with 25% laser (561) power at 100 msec. Each sample was imaged no longer than 15 mins. Each technical replicate consisted of movies from at least two fields of view containing between 5 and 10 microtubules each.

Single-molecule motility assay analysis

Kymographs were generated from motility movies and quantified for run lengths, percent motility, and velocity using ImageJ (NIH). Specifically, maximum-intensity projections were generated from time-lapse sequences to define the trajectory of particles on a single microtubule. The segmented line tool was used to trace the trajectories and map them onto the original video sequence, which was subsequently re-sliced to generate a kymograph. Motile and immotile events (> 1 sec) were manually traced. Bright aggregates, which were less than 5% of

the population, were excluded from the analysis. For dynein-dynactin-NINL, both stationary and diffusive events were grouped as immotile. Run length measurements were calculated from motile events only. For percent motility per microtubule measurements, motile events (> 1 sec and > 1μm) were divided by total events per kymograph. Velocity measurements were calculated from the inverse slopes of the motile event traces (> 1 sec and > 1μm) only. Statistical analyses were performed in Prism8 (Graphpad).

Western blot analysis

293T cells were maintained in Dulbecco's modified Eagle's medium (containing 10% fetal bovine serum and 1% penicillin/streptomycin). For Western blot quantification of LRRK2 protein expression (Extended Data Fig. 15), cells were plated on 6-well dishes (150K cells per well) 24 hrs before transfection. Cells were transfected with 1 μg of GFP-I2020T using polyethylenimine (PEI, Polysciences). After 48 hrs, cells were treated for 30 mins with either 5 μM GZD-824 or DMSO-matched control. Cells were lysed on ice in RIPA buffer (50 mM Tris pH 7.5, 150 mM NaCl, 0.2% TritonX-10, 0.1%SDS, 0.5% Na-Deoxycholate, with cOmplete protease inhibitor cocktail). Lysates were further rotated for 15 mins at 4°C and clarified by centrifuging at 13,000 x g for 15 mins. Clarified supernatants were boiled for 5 mins in Laemmli buffer. The experiments were performed in triplicate.

For Western blots, lysates were run on 4-12% gradient SDS-PAGE (Life Technologies) for 60 mins and transferred to nitrocellulose for 3 hrs at 250 mA. Blots were dried at RT for 30 mins, rinsed in 1x Tris buffered saline (TBS), followed by blocking with 5% milk in TBS. Antibodies were diluted in 5% milk in TBS-0.1% Tween-20 (TBS-T). Primary antibodies were incubated overnight at 4°C and Infrared (IR) secondary antibodies were incubated at RT for 45 mins. For quantification of LRRK2 expression levels, blots were imaged on an Odyssey CLx controlled by Imaging Studio software (v5.2). DMSO and GZD-824 conditions were quantified in

triplicate and normalized to a GAPDH loading control using Empiria Studio software (Li-COR). To ensure quantification was in the combined linear range for antibodies detecting both GFP-LRRK2 and GAPDH, a linear dilution series of lysates from cells expressing GFP-LRRK2 was also quantified by IR Western blot.

Immunofluorescence, confocal microscopy and image analysis

The day before transfection, 293T cells were plated on acid-treated coverslips (Bellco Glass) pre-coated with 100 µg/mL Poly-D-lysine (Sigma) and 4 µg/mL Mouse Laminin (ThermoFisher) in 24-well plates (35K cells per well). Cells were transfected with 500 ng plasmid of either pDEST53-GFP-LRRK2 or pDEST53-GFP-LRRK2(I2020T) using PEI. After 48-72 hrs, cells were incubated with either a kinase inhibitor or DMSO-matched control (matched for time and concentration). For the Type 1 inhibitor experiment, cells were incubated with DMSO or Mli-2 (500 nM) for 2 hrs. For the Type 2 inhibitor, cells were incubated with DMSO or GZD-824 (5 or 10 µM) for 30 mins. Cells were quickly washed 1x on ice with ice-cold PBS, and fixed with ice-cold 4%PFA/90%Methanol/5mM sodium bicarbonate for 10 mins at -20°C. Following fixation, the wells were immediately washed 3x with ice-cold PBS. Blocking buffer (1% BSA, 5% normal goat serum, 0.3%TritonX-100 in PBS) was added for 1 hr at RT. Primary antibodies were diluted (1:500) in antibody dilution buffer (1% BSA, 0.1% TritonX-100 in PBS) and incubated overnight at 4°C. After overnight incubation, the wells were washed 3x in PBS and incubated with secondary antibodies (1:500) in antibody dilution buffer for 1 hr at RT. After secondary incubation, the wells were washed 3x in PBS, 1x in ddH2O and mounted using CitiFluor AF2 (EMS) on Superfrost Plus Microscope slides (ThermoFisher). Coverslips were sealed with nail polish and stored at 4°C.

For the LRRK2 filament analysis in Fig. 5, experimenters were blinded to condition for both the imaging acquisition and analysis. Cells were imaged using a Nikon A1R HD confocal

microscope with a LUN-V laser engine (405nm, 488nm, 561nm, and 640nm) and DU4 detector using bandpass and longpass filters for each channel (450/50, 525/50, 595/50, and 700/75). Slides were imaged on a Nikon Ti2 body using an Apo 60x 1.49 NA objective. Image stacks were acquired in resonant scanning mode with bidirectional scanning and 4x line averaging and 1.2 airy units. The lasers used were 405 nm, 488 nm and 561 nm. Illumination and image acquisition were controlled by NIS Elements Advanced Research software (Nikon Instruments). ImageJ was used to quantify the percent of cells with LRRK2 filaments. Maximum-intensity projections were generated from z-stack confocal images. Using the GFP immunofluorescence signal, transfected cells were traced. Cells were scored for the presence or absence of filaments using both the z-projection and z-stack micrographs as a guide. The presence of filaments was scored if the cells had either (a) a GFP filament signal greater than 5 μm or (b) bundles of filaments with at least two identifiable crosses. To calculate the percent cells with filaments, the number of cells with filaments was divided by the total number of transfected cells per technical (defined as one 24-well coverslip). Approximately 20 cells were quantified per replicate for each condition in Figure 5D (DMSO v. Mli-2) and between 40-100 cells were quantified per replicate for each condition in Figure 5F (DMSO v. GZD-824). The quantification of all cellular experiments comes from data collected on three separate days except for the 10 μM GZD-824 condition in Figure 5F which was performed on two separate days. All statistical analyses were performed in Prism8 (Graphpad).

REFERENCES

1. Monfrini, E. & Di Fonzo, A. Leucine-Rich Repeat Kinase (LRRK2) Genetics and Parkinson's Disease. Adv Neurobiol 14, 3–30 (2017).

2. Di Maio, R., Hoffman, E. K., Rocha, E. M., Keeney, M. T., Sanders, L. H., De Miranda, B. R., Zharikov, A., Van Laar, A., Stepan, A. F., Lanz, T. A., Kofler, J. K., Burton, E. A., Alessi, D. R., Hastings, T. G. & Greenamyre, J. T. LRRK2 activation in idiopathic Parkinson's disease. Sci Transl Med 10, eaar5429 (2018).

3. Hui, K. Y., Fernandez-Hernandez, H., Hu, J., Schaffner, A., Pankratz, N., Hsu, N.-Y., Chuang, L.-S., Carmi, S., Villaverde, N., Li, X., Rivas, M., Levine, A. P., Bao, X., Labrias, P. R., Haritunians, T., Ruane, D., Gettler, K., Chen, E., Li, D., Schiff, E. R., Pontikos, N., Barzilai, N., Brant, S. R., Bressman, S., Cheifetz, A. S., Clark, L. N., Daly, M. J., Desnick, R. J., Duerr, R. H., Katz, S., Lencz, T., Myers, R. H., Ostrer, H., Ozelius, L., Payami, H., Peter, Y., Rioux, J. D., Segal, A. W., Scott, W. K., Silverberg, M. S., Vance, J. M., Ubarretxena-Belandia, I., Foroud, T., Atzmon, G., Pe'er, I., Ioannou, Y., McGovern, D. P. B., Yue, Z., Schadt, E. E., Cho, J. H. & Peter, I. Functional variants in the LRRK2 gene confer shared effects on risk for Crohn‘s disease and Parkinson’s disease. Sci Transl Med 10, eaai7795 (2018).

4. Barrett, J. C., Hansoul, S., Nicolae, D. L., Cho, J. H., Duerr, R. H., Rioux, J. D., Brant, S. R., Silverberg, M. S., Taylor, K. D., Barmada, M. M., Bitton, A., Dassopoulos, T., Datta, L. W., Green, T., Griffiths, A. M., Kistner, E. O., Murtha, M. T., Regueiro, M. D., Rotter, J. I., Schumm, L. P., Steinhart, A. H., Targan, S. R., Xavier, R. J., NIDDK IBD Genetics Consortium, Libioulle, C., Sandor, C., Lathrop, M., Belaiche, J., Dewit, O., Gut, I., Heath, S., Laukens, D., Mni, M., Rutgeerts, P., Van Gossum, A., Zelenika, D., Franchimont, D., Hugot, J.-P., de Vos, M., Vermeire, S., Louis, E., Belgian-French IBD Consortium, Wellcome Trust Case Control Consortium, Cardon, L. R., Anderson, C. A., Drummond, H., Nimmo, E., Ahmad, T., Prescott, N. J., Onnie, C. M., Fisher, S. A., Marchini, J., Ghori, J., Bumpstead, S., Gwilliam, R., Tremelling, M., Deloukas, P., Mansfield, J., Jewell, D., Satsangi, J., Mathew, C. G., Parkes, M., Georges, M. & Daly, M. J. Genome-wide association defines more than 30 distinct susceptibility loci for Crohn's disease. Nat. Genet. 40, 955–962 (2008).

5. Schurr, E. & Gros, P. A common genetic fingerprint in leprosy and Crohn's disease? N. Engl. J. Med. 361, 2666–2668 (2009).

6. Abeliovich, A. & Gitler, A. D. Defects in trafficking bridge Parkinson's disease pathology and genetics. Nature 539, 207–216 (2016).

7. Kluss, J. H., Mamais, A. & Cookson, M. R. LRRK2 links genetic and sporadic Parkinson's disease. Biochem Soc Trans 47, 651–661 (2019).

8. Steger, M., Tonelli, F., Ito, G., Davies, P., Trost, M., Vetter, M., Wachter, S., Lorentzen, E., Duddy, G., Wilson, S., Baptista, M. A., Fiske, B. K., Fell, M. J., Morrow, J. A., Reith, A. D., Alessi, D. R. & Mann, M. Phosphoproteomics reveals that Parkinson's disease kinase LRRK2 regulates a subset of Rab GTPases. elife 5, 809 (2016).

9. Steger, M., Diez, F., Dhekne, H. S., Lis, P., Nirujogi, R. S., Karayel, O., Tonelli, F., Martinez, T. N., Lorentzen, E., Pfeffer, S. R., Alessi, D. R. & Mann, M. Systematic proteomic analysis of LRRK2-mediated Rab GTPase phosphorylation establishes a connection to ciliogenesis. elife 6, e80705 (2017).

10. Reck-Peterson, S. L., Redwine, W. B., Vale, R. D. & Carter, A. P. The cytoplasmic dynein transport machinery and its many cargoes. Nat Rev Mol Cell Biol 149, 1–17 (2018).

11. Guedes-Dias, P. & Holzbaur, E. L. F. Axonal transport: Driving synaptic function. Science 366, (2019).

12. Gloeckner, C. J., Kinkl, N., Schumacher, A., Braun, R. J., O'Neill, E., Meitinger, T., Kolch, W., Prokisch, H. & Ueffing, M. The Parkinson disease causing LRRK2 mutation I2020T is associated with increased kinase activity. Hum. Mol. Genet. 15, 223–232 (2006).

13. Kett, L. R., Boassa, D., Ho, C. C.-Y., Rideout, H. J., Hu, J., Terada, M., Ellisman, M. & Dauer, W. T. LRRK2 Parkinson disease mutations enhance its microtubule association. Hum. Mol. Genet. 21, 890–899 (2012).

14. Gotthardt, K., Weyand, M., Kortholt, A., Van Haastert, P. J. M. & Wittinghofer, A. Structure of the Roc-COR domain tandem of C. tepidum, a prokaryotic homologue of the human LRRK2 Parkinson kinase. EMBO J 27, 2239–2249 (2008).

15. Deyaert, E., Leemans, M., Singh, R. K., Gallardo, R., Steyaert, J., Kortholt, A., Lauer, J. & Versées, W. Structure and nucleotide-induced conformational dynamics of the Chlorobium tepidum Roco protein. Biochem. J. 476, 51–66 (2019).

16. Gilsbach, B. K., Ho, F. Y., Vetter, I. R., Van Haastert, P. J. M., Wittinghofer, A. & Kortholt, A. Roco kinase structures give insights into the mechanism of Parkinson disease-related leucine-rich-repeat kinase 2 mutations. Proc Natl Acad Sci USA 109, 10322–10327 (2012).

17. Deng, J., Lewis, P. A., Greggio, E., Sluch, E., Beilina, A. & Cookson, M. R. Structure of the ROC domain from the Parkinson's disease-associated leucine-rich repeat kinase 2 reveals a dimeric GTPase. Proc Natl Acad Sci USA 105, 1499–1504 (2008).

18. Zhang, P., Fan, Y., Ru, H., Wang, L., Magupalli, V. G., Taylor, S. S., Alessi, D. R. & Wu, H. Crystal structure of the WD40 domain dimer of LRRK2. Proc Natl Acad Sci USA 116, 1579–1584 (2019).

19. Guaitoli, G., Raimondi, F., Gilsbach, B. K., Gómez-Llorente, Y., Deyaert, E., Renzi, F., Li, X., Schaffner, A., Jagtap, P. K. A., Boldt, K., Zweydorf, von, F., Gotthardt, K., Lorimer, D. D., Yue, Z., Burgin, A., Janjic, N., Sattler, M., Versées, W., Ueffing, M., Ubarretxena-Belandia, I., Kortholt, A. & Gloeckner, C. J. Structural model of the dimeric Parkinson's protein LRRK2 reveals a compact architecture involving distant interdomain contacts. Proc Natl Acad Sci USA 113, E4357–66 (2016).

20. Sejwal, K., Chami, M., Rémigy, H., Vancraenenbroeck, R., Sibran, W., Sütterlin, R., Baumgartner, P., McLeod, R., Chartier-Harlin, M.-C., Baekelandt, V., Stahlberg, H. & Taymans, J.-M. Cryo-EM analysis of homodimeric full-length LRRK2 and LRRK1 protein complexes. Sci Rep 7, 8667 (2017).

21. Watanabe, R., Buschauer, R., Bohning, J., Audagnotto, M., Lasker, K., Lu, T. W., Boassa, D., Taylor, S. S. & Villa, E. The *in situ* structure of Parkinson's disease-linked LRRK2. bioRxiv 1–22 (2019). doi:10.1101/837203

22. Wang, R. Y.-R., Song, Y., Barad, B. A., Cheng, Y., Fraser, J. S. & DiMaio, F. Automated structure refinement of macromolecular assemblies from cryo-EM maps using Rosetta. elife 5, 352 (2016).

23. Emsley, P. & Cowtan, K. Coot: model-building tools for molecular graphics. Acta Crystallographica Section D: Biological Crystallography 60, 2126–2132 (2004).

24. Ito, G., Okai, T., Fujino, G., Takeda, K., Ichijo, H., Katada, T. & Iwatsubo, T. GTP binding is essential to the protein kinase activity of LRRK2, a causative gene product for familial Parkinson's disease. Biochemistry 46, 1380–1388 (2007).

25. West, A. B., Moore, D. J., Choi, C., Andrabi, S. A., Li, X., Dikeman, D., Biskup, S., Zhang, Z., Lim, K.-L., Dawson, V. L. & Dawson, T. M. Parkinson's disease-associated mutations in LRRK2 link enhanced GTP-binding and kinase activities to neuronal toxicity. Hum. Mol. Genet. 16, 223–232 (2007).

26. Terheyden, S., Nederveen-Schippers, L. M. & Kortholt, A. The unconventional G-protein cycle of LRRK2 and Roco proteins. Biochem Soc Trans 44, 1611–1616 (2016).

27. Lietha, D., Cai, X., Ceccarelli, D. F. J., Li, Y., Schaller, M. D. & Eck, M. J. Structural basis for the autoinhibition of focal adhesion kinase. Cell 129, 1177–1187 (2007).

28. Terheyden, S., Ho, F. Y., Gilsbach, B. K., Wittinghofer, A. & Kortholt, A. Revisiting the Roco G-protein cycle. Biochem. J. 465, 139–147 (2015).

29. Cheng, K.-Y., Noble, M. E. M., Skamnaki, V., Brown, N. R., Lowe, E. D., Kontogiannis, L., Shen, K., Cole, P. A., Siligardi, G. & Johnson, L. N. The role of the phospho-CDK2/cyclin A recruitment site in substrate recognition. J Biol Chem 281, 23167–23179 (2006).

30. Schmidt, S. H., Knape, M. J., Boassa, D., Mumdey, N., Kornev, A. P., Ellisman, M. H., Taylor, S. S. & Herberg, F. W. The dynamic switch mechanism that leads to activation of LRRK2 is embedded in the DFGψ motif in the kinase domain. Proc Natl Acad Sci USA 116, 14979–14988 (2019).

31. Pungaliya, P. P., Bai, Y., Lipinski, K., Anand, V. S., Sen, S., Brown, E. L., Bates, B., Reinhart, P. H., West, A. B., Hirst, W. D. & Braithwaite, S. P. Identification and characterization of a leucine-rich repeat kinase 2 (LRRK2) consensus phosphorylation motif. PLoS ONE 5, e13672 (2010).

32. Case, R. B., Pierce, D. W., Hom-Booher, N., Hart, C. L. & Vale, R. D. The directional preference of kinesin motors is specified by an element outside of the motor catalytic domain. Cell 90, 959–966 (1997).

33. Redwine, W. B., DeSantis, M. E., Hollyer, I., Htet, Z. M., Tran, P. T., Swanson, S. K., Florens, L., Washburn, M. P. & Reck-Peterson, S. L. The human cytoplasmic dynein interactome reveals novel activators of motility. elife 6, 379 (2017).

34. Liu, M., Bender, S. A., Cuny, G. D., Sherman, W., Glicksman, M. & Ray, S. S. Type II kinase inhibitors show an unexpected inhibition mode against Parkinson's disease-linked LRRK2 mutant G2019S. Biochemistry 52, 1725–1736 (2013).

35. Canning, P., Ruan, Q., Schwerd, T., Hrdinka, M., Maki, J. L., Saleh, D., Suebsuwong, C., Ray, S., Brennan, P. E., Cuny, G. D., Uhlig, H. H., Gyrd-Hansen, M., Degterev, A. &

Bullock, A. N. Inflammatory Signaling by NOD-RIPK2 Is Inhibited by Clinically Relevant Type II Kinase Inhibitors. Chemistry & biology 22, 1174–1184 (2015).

36. Ren, X., Pan, X., Zhang, Z., Wang, D., Lu, X., Li, Y., Wen, D., Long, H., Luo, J., Feng, Y., Zhuang, X., Zhang, F., Liu, J., Leng, F., Lang, X., Bai, Y., She, M., Tu, Z., Pan, J. & Ding, K. Identification of GZD824 as an orally bioavailable inhibitor that targets phosphorylated and nonphosphorylated breakpoint cluster region-Abelson (Bcr-Abl) kinase and overcomes clinically acquired mutation-induced resistance against imatinib. J. Med. Chem. 56, 879–894 (2013).

37. Scott, J. D., DeMong, D. E., Greshock, T. J., Basu, K., Dai, X., Harris, J., Hruza, A., Li, S. W., Lin, S.-I., Liu, H., Macala, M. K., Hu, Z., Mei, H., Zhang, H., Walsh, P., Poirier, M., Shi, Z.-C., Xiao, L., Agnihotri, G., Baptista, M. A. S., Columbus, J., Fell, M. J., Hyde, L. A., Kuvelkar, R., Lin, Y., Mirescu, C., Morrow, J. A., Yin, Z., Zhang, X., Zhou, X., Chang, R. K., Embrey, M. W., Sanders, J. M., Tiscia, H. E., Drolet, R. E., Kern, J. T., Sur, S. M., Renger, J. J., Bilodeau, M. T., Kennedy, M. E., Parker, E. M., Stamford, A. W., Nargund, R., McCauley, J. A. & Miller, M. W. Discovery of a 3-(4-Pyrimidinyl) Indazole (MLi-2), an Orally Available and Selective Leucine-Rich Repeat Kinase 2 (LRRK2) Inhibitor that Reduces Brain Kinase Activity. J. Med. Chem. 60, 2983–2992 (2017).

38. Fell, M. J., Mirescu, C., Basu, K., Cheewatrakoolpong, B., DeMong, D. E., Ellis, J. M., Hyde, L. A., Lin, Y., Markgraf, C. G., Mei, H., Miller, M., Poulet, F. M., Scott, J. D., Smith, M. D., Yin, Z., Zhou, X., Parker, E. M., Kennedy, M. E. & Morrow, J. A. MLi-2, a Potent, Selective, and Centrally Active Compound for Exploring the Therapeutic Potential and Safety of LRRK2 Kinase Inhibition. J. Pharmacol. Exp. Ther. 355, 397–409 (2015).

39. Deng, X., Dzamko, N., Prescott, A., Davies, P., Liu, Q., Yang, Q., Lee, J.-D., Patricelli, M. P., Nomanbhoy, T. K., Alessi, D. R. & Gray, N. S. Characterization of a selective inhibitor of the Parkinson's disease kinase LRRK2. Nat. Chem. Biol. 7, 203–205 (2011).

40. Gilsbach, B. K., Messias, A. C., Ito, G., Sattler, M., Alessi, D. R., Wittinghofer, A. & Kortholt, A. Structural Characterization of LRRK2 Inhibitors. J. Med. Chem. 58, 3751–3756 (2015).

41. Godena, V. K., Brookes-Hocking, N., Moller, A., Shaw, G., Oswald, M., Sancho, R. M., Miller, C. C. J., Whitworth, A. J. & De Vos, K. J. Increasing microtubule acetylation rescues axonal transport and locomotor deficits caused by LRRK2 Roc-COR domain mutations. Nat Commun 5, 5245 (2014).

42. Blanca Ramírez, M., Lara Ordóñez, A. J., Fdez, E., Madero-Pérez, J., Gonnelli, A., Drouyer, M., Chartier-Harlin, M.-C., Taymans, J.-M., Bubacco, L., Greggio, E. & Hilfiker, S. GTP binding regulates cellular localization of Parkinson's disease-associated LRRK2. Hum. Mol. Genet. 26, 2747–2767 (2017).

43. Dixit, R., Ross, J. L., Goldman, Y. E. & Holzbaur, E. L. F. Differential regulation of dynein and kinesin motor proteins by tau. 319, 1086–1089 (2008).

44. Reck-Peterson, S., Yildiz, A., Carter, A., Gennerich, A., Zhang, N. & Vale, R. Single-molecule analysis of dynein processivity and stepping behavior. Cell 126, 335–348 (2006).

45. Qiu, W., Derr, N. D., Goodman, B. S., Villa, E., Wu, D., Shih, W. & Reck-Peterson, S. L. Dynein achieves processive motion using both stochastic and coordinated stepping. Nat Struct Mol Biol 19, 193–200 (2012).

46. DeWitt, M. A., Chang, A. Y., Combs, P. A. & Yildiz, A. Cytoplasmic dynein moves through uncoordinated stepping of the AAA+ ring domains. 335, 221–225 (2012).

47. Wang, Y., Huynh, W., Skokan, T. D., Lu, W., Weiss, A. & Vale, R. D. CRACR2a is a calcium-activated dynein adaptor protein that regulates endocytic traffic. J Cell Biol 218, 1619–1633 (2019).

48. Etoh, K. & Fukuda, M. Rab10 regulates tubular endosome formation through KIF13A and KIF13B motors. J Cell Sci 132, (2019).

49. Horgan, C. P., Hanscom, S. R., Jolly, R. S., Futter, C. E. & McCaffrey, M. W. Rab11-FIP3 links the Rab11 GTPase and cytoplasmic dynein to mediate transport to the endosomal-recycling compartment. J Cell Sci 123, 181–191 (2010).

50. Niwa, S., Tanaka, Y. & Hirokawa, N. KIF1Bbeta- and KIF1A-mediated axonal transport of presynaptic regulator Rab3 occurs in a GTP-dependent manner through DENN/MADD. Nat Cell Biol 10, 1269–1279 (2008).

51. Matanis, T., Akhmanova, A., Wulf, P., Del Nery, E., Weide, T., Stepanova, T., Galjart, N., Grosveld, F., Goud, B., De Zeeuw, C. I., Barnekow, A. & Hoogenraad, C. C. Bicaudal-D regulates COPI-independent Golgi-ER transport by recruiting the dynein-dynactin motor complex. Nat Cell Biol 4, 986–992 (2002).

52. Blanca Ramírez, M., Lara Ordóñez, A. J., Fdez, E. & Hilfiker, S. LRRK2: from kinase to GTPase to microtubules and back. Biochem Soc Trans 45, 141–146 (2017).

53. Sui, H. & Downing, K. H. Structural basis of interprotofilament interaction and lateral deformation of microtubules. Structure 18, 1022–1031 (2010).

54. Charrier, J.-D., Miller, A., Kay, D. P., Brenchley, G., Twin, H. C., Collier, P. N., Ramaya, S., Keily, S. B., Durrant, S. J., Knegtel, R. M. A., Tanner, A. J., Brown, K., Curnock, A. P. & Jimenez, J.-M. Discovery and structure-activity relationship of 3-aminopyrid-2-ones as potent and selective interleukin-2 inducible T-cell kinase (Itk) inhibitors. J. Med. Chem. 54, 2341–2350 (2011).

55. Pellegrini, E., Signor, L., Singh, S., Boeri Erba, E. & Cusack, S. Structures of the inactive and active states of RIP2 kinase inform on the mechanism of activation. PLoS ONE 12, e0177161 (2017).

56. Greggio, E., Jain, S., Kingsbury, A., Bandopadhyay, R., Lewis, P., Kaganovich, A., van der Brug, M. P., Beilina, A., Blackinton, J., Thomas, K. J., Ahmad, R., Miller, D. W., Kesavapany, S., Singleton, A., Lees, A., Harvey, R. J., Harvey, K. & Cookson, M. R. Kinase activity is required for the toxic effects of mutant LRRK2/dardarin. Neurobiology of Disease 23, 329–341 (2006).

57. Woehlke, G., Ruby, A. K., Hart, C. L., Ly, B., Hom-Booher, N. & Vale, R. D. Microtubule interaction site of the kinesin motor. Cell 90, 207–216 (1997).

58. Suloway, C., Pulokas, J., Fellmann, D., Cheng, A., Guerra, F., Quispe, J., Stagg, S., Potter, C. S. & Carragher, B. Automated molecular microscopy: the new Leginon system. 151, 41–60 (2005).

59. Zheng, S. Q., Palovcak, E., Armache, J.-P., Verba, K. A., Cheng, Y. & Agard, D. A. MotionCor2: anisotropic correction of beam-induced motion for improved cryo-electron microscopy. Nature Methods 14, 331–332 (2017).

60. Zhang, K. Gctf: Real-time CTF determination and correction. J. Struct. Biol. 193, 1–12 (2016).

61. Lander, G., Stagg, S., Voss, N., Cheng, A., Fellmann, D., Pulokas, J., Yoshioka, C., Irving, C., Mulder, A. & Lau, P. Appion: an integrated, database-driven pipeline to facilitate EM image processing. 166, 95–102 (2009).

62. Roseman, A. M. FindEM--a fast, efficient program for automatic selection of particles from electron micrographs. J. Struct. Biol. 145, 91–99 (2004).

63. Zivanov, J., Nakane, T., Forsberg, B., Kimanius, D., Hagen, W. J. H., Lindahl, E. & Scheres, S. H. W. RELION-3: new tools for automated high-resolution cryo-EM structure determination. 1–38 (2018). doi:10.1101/421123

64. Punjani, A., Rubinstein, J. L., Fleet, D. J. & Brubaker, M. A. cryoSPARC: algorithms for rapid unsupervised cryo-EM structure determination. Nature Methods (2017). doi:10.1038/nmeth.4169

65. Henderson, R., Sali, A., Baker, M. L., Carragher, B., Devkota, B., Downing, K. H., Egelman, E. H., Feng, Z., Frank, J., Grigorieff, N., Jiang, W., Ludtke, S. J., Medalia, O., Penczek, P. A., Rosenthal, P. B., Rossmann, M. G., Schmid, M. F., Schröder, G. F., Steven, A. C., Stokes, D. L., Westbrook, J. D., Wriggers, W., Yang, H., Young, J., Berman, H. M., Chiu, W., Kleywegt, G. J. & Lawson, C. L. Outcome of the first electron microscopy validation task force meeting. in Structure 20, 205–214 (2012).

66. Scheres, S. H. W. & Chen, S. Prevention of overfitting in cryo-EM structure determination. Nature Methods 9, 853–854 (2012).

67. Chen, S., McMullan, G., Faruqi, A. R., Murshudov, G. N., Short, J. M., Scheres, S. H. W. & Henderson, R. High-resolution noise substitution to measure overfitting and validate resolution in 3D structure determination by single particle electron cryomicroscopy. Ultramicroscopy 135C, 24–35 (2013).

68. Emsley, P., Lohkamp, B., Scott, W. G. & Cowtan, K. Features and development of Coot. Acta Crystallographica Section D: Biological Crystallography 66, 486–501 (2010).

69. Söding, J., Biegert, A. & Lupas, A. N. The HHpred interactive server for protein homology detection and structure prediction. Nucleic Acids Res 33, W244–8 (2005).

70. Greggio, E., Taymans, J.-M., Zhen, E. Y., Ryder, J., Vancraenenbroeck, R., Beilina, A., Sun, P., Deng, J., Jaffe, H., Baekelandt, V., Merchant, K. & Cookson, M. R. The Parkinson's disease kinase LRRK2 autophosphorylates its GTPase domain at multiple sites. Biochemical and Biophysical Research Communications 389, 449–454 (2009).

71. Wagner, T., Merino, F., Stabrin, M., Moriya, T., Gatsogiannis, C. & Raunser, S. SPHIRE-crYOLO: A fast and well-centering automated particle picker for cryo-EM. 1–25 (2018). doi:10.1101/356584

72. Lis, P., Burel, S., Steger, M., Mann, M., Brown, F., Diez, F., Tonelli, F., Holton, J. L., Ho, P. W., Ho, S.-L., Chou, M.-Y., Polinski, N. K., Martinez, T. N., Davies, P. & Alessi, D. R. Development of phospho-specific Rab protein antibodies to monitor *in vivo* activity of the LRRK2 Parkinson's disease kinase. Biochem. J. 475, 1–22 (2018).

73. Nicholas, M. P., Rao, L. & Gennerich, A. An improved optical tweezers assay for measuring the force generation of single kinesin molecules. Methods Mol Biol 1136, 171–246 (2014).

74. Htet, Z. M., Gillies, J. P., Baker, R. W., Leschziner, A. E., DeSantis, M. E. & Reck-Peterson, S. L. Lis1 promotes the formation of maximally activated cytoplasmic dynein-1 complexes. bioRxiv 19, 1–30 (2019).

FIGURES

Figure 1 | Cryo-EM structure of LRRK2^{RCKW}. a, Schematic of the construct used in this study, with amino acid numbers of the beginning and end indicated. The N-terminal half of LRRK2, absent from our construct, is shown in dim colors. The same color-coding of domains is used throughout the paper. The five major familial Parkinson's Disease mutations and a Crohn's Disease-linked mutation are indicated below the diagram. **b**, 3.5Å map of the LRRK2^{RCKW} trimer, with one monomer highlighted using the colors shown in (a). **c**, Local resolution of the map shown in (b). **d**, Density for a LRRK2^{RCKW} monomer obtained after processing data where the RoC and COR-A domains were signal-subtracted from two of the monomers in each trimer (see Methods and Extended Data Fig. 2 for details). **e**, Local resolution for the monomer in (d), showing the improvements in the RoC and COR-A domains. **f**, Ribbon diagram of the atomic model of LRRK2^{RCKW}. **g**, An 8.1Å cryo-EM map of monomeric LRRK2^{RCKW} with the atomic model built from the trimer docked in. **h**, Close up of the area highlighted by the dashed box in (g). **i**, Each LRRK2^{RCKW} domain is highlighted in color in the context of an otherwise grey ribbon representation of the full structure. **j**, **k**, Location of the Parkinson's and Crohn's Disease mutations listed in (a). **l**, Interface between the C-terminal helix and the kinase domain in LRRK2^{RCKW}. **m**, details of the electrostatic and hydrophobic interactions found at that interface, with the residues involved indicated.

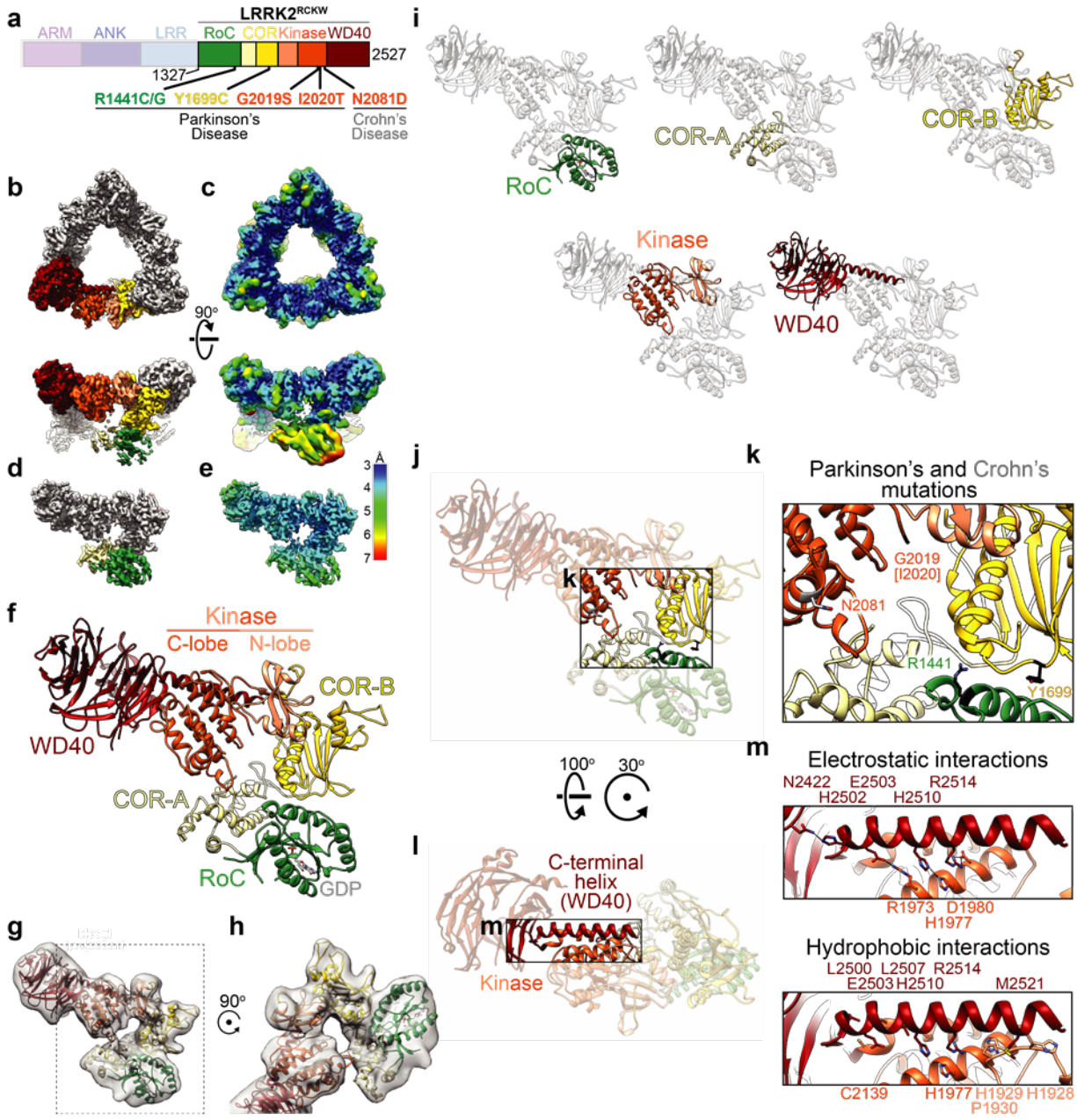
a
LRRK2RCKW
ARM ANK LRR RoC COR Kinase WD40
2527
1327
R1441C/G Y1699C G2019S I2020T N2081D
Parkinson's Disease
Crohn's Disease
b
c
90°
d
e
3 Å
4
5
6
7
f
Kinase
C-lobe N-lobe
COR-B
WD40
COR-A
RoC
GDP
g
h
90°
i
RoC
COR-A
COR-B
Kinase
WD40
j
k
100°
30°
l
C-terminal helix (WD40)
m
Kinase
k
Parkinson's and Crohn's mutations
G2019 [I2020]
N2081
R1441
Y1699
m
Electrostatic interactions
N2422 E2503 R2514
H2502 H2510
R1973 D1980
H1977
Hydrophobic interactions
L2500 L2507 R2514
E2503 H2510 M2521
C2139 H1977 H1929 H1928
P1930

Figure 2 | Modeling the microtubule-associated LRRK2 filaments. a, 14Å sub-tomogram average of a segment of microtubule-associated LRRK2 filament in cells. The microtubule is shown in blue and the LRRK2 filament in grey. **b**, Cryo-EM of microtubule-associated LRRK2^{RCKW} filaments reconstituted *in vitro* using purified LRRK2^{RCKW} and purified microtubules. The blue square brackets indicate the boundaries of the microtubule, and the arrowheads point to examples of LRRK2^{RCKW} filaments. **c**, Fitting of the LRRK2^{RCKW} structure, which has its kinase in an open conformation, into the sub-tomogram average. **d**, Atomic model of the LRRK2^{RCKW} filaments (c) with the sub-tomogram average density removed. The white circles highlight the filament interface mediated by interactions between COR domains, where clashes are found. **e**, Magnified views of the circled area shown in (d). **f**, Superposition of the LRRK2^{RCKW} structure (colored by domains) and a model of LRRK2^{RCKW} with its kinase in a closed conformation in blue (see Methods and Extended Data Fig. 6f-j for details on the model building). The dashed blue arrow indicates the general direction of movement upon closing of the kinase. **g**, Fitting of the closed-kinase model of LRRK2^{RCKW} into the sub-tomogram average. **h**, Atomic model of the closed-kinase LRRK2^{RCKW} filaments (g) with the sub-tomogram average density removed and a white circle highlighting the same interface as in (d). **i**, Magnified views of the circled area shown in (h). **j**, **k**, Cartoon representation of the two filament models, highlighting the clashes observed with open-kinase LRRK2^{RCKW} (j) and resolved with the closed-kinase model (k). Backbone clashes in (d, e) and (h, i) were measured in Chimera with Find Clashes using a poly-alanine model of LRRK2^{RCKW}. There were 997 clashes in the filament modeled using our LRRK2^{RCKW} structure (“open” form (d, e)) and 184 clashes in the filament built using the closed-kinase model of LRRK2^{RCKW} (h, i), corresponding to an overall reduction of 81.8% in the number of clashes.

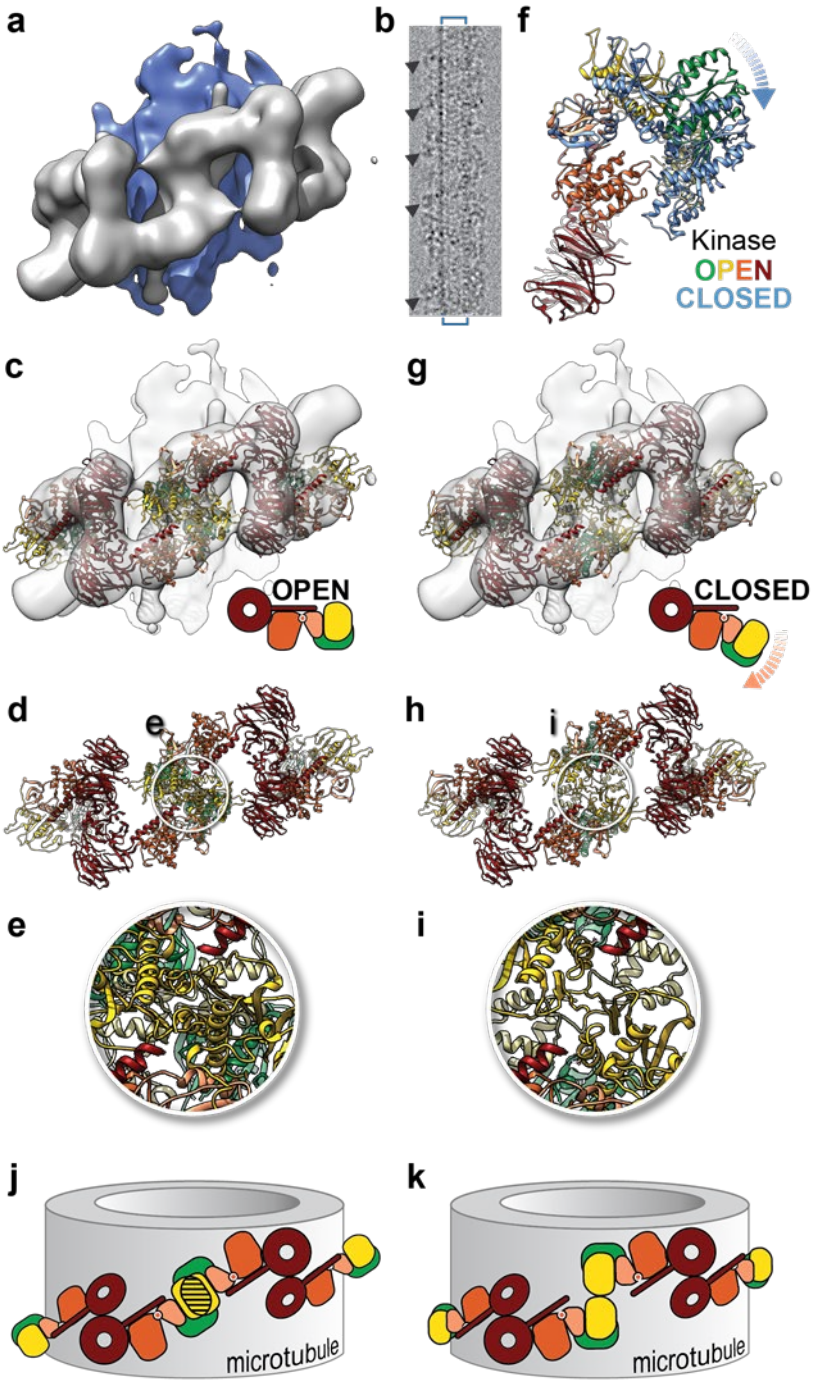
a
b
f
Kinase
OPEN
CLOSED
c
OPEN
g
CLOSED
d
e
h
i
e
i
j
microtubule
k
microtubule

Figure 3 | LRRK2^{RCKW} forms WD40- and COR-mediated dimers outside the filaments. a-d, The same filament model shown in Fig. 2j, k is shown here in grey, with either a WD40-mediated (a), or COR-mediated (c) LRRK2^{RCKW} dimer highlighted with domain colors. The corresponding molecular models are shown next to the cartoons (b, d). **e**, **f**, Cryo-EM reconstructions of LRRK2^{RCKW} dimers obtained in the absence of inhibitor ("Apo"), or in the presence of MLi-2. The molecular models (left) are the same ones shown in (b, d) for the WD40-mediated (e) and COR-mediated (f) LRRK2^{RCKW} dimers. The models are shown in an orientation that matches the cryo-EM maps shown in the first column. For each reconstruction, two orientations of the map are shown: down the two-fold axis at the dimerization interface (left), and perpendicular to it (right). For each species, the top row shows the cryo-EM map and the bottom row a transparent version of the map with a model docked in. The models docked into the maps obtained in the presence of MLi-2 are those derived from building the filaments (Fig. 2g-i). Those docked into the maps obtained in the absence of inhibitor were built with the LRRK2^{RCKW} structure (i.e. with an open kinase) but maintaining the interfaces identified in the filaments. Both types of dimers were also observed in the presence of Ponatinib but the preferred orientation of the sample prevented us from obtaining a 3D reconstruction; Extended Data Fig. 10 shows 2D class averages instead. **g**, We built molecular models of the WD40-mediated and COR-mediated dimers of LRRK2^{RCKW} obtained in the presence of MLi-2 (e, f) by fitting the two halves of LRRK2^{RCKW} split at the junction between the N- and C-lobes of the kinase (see Extended Data Fig. 11). We then aligned, in alternating order, copies of these dimers. This panel shows the resulting right-handed helix. **h**, **i**, The helix has dimensions compatible with the diameter of a 12-protofilament microtubule (EMD-5192)[53], which was the species used to obtain the tomographic reconstruction shown in Fig. 2a[21], and has its RoC domains pointing towards the microtubule surface.

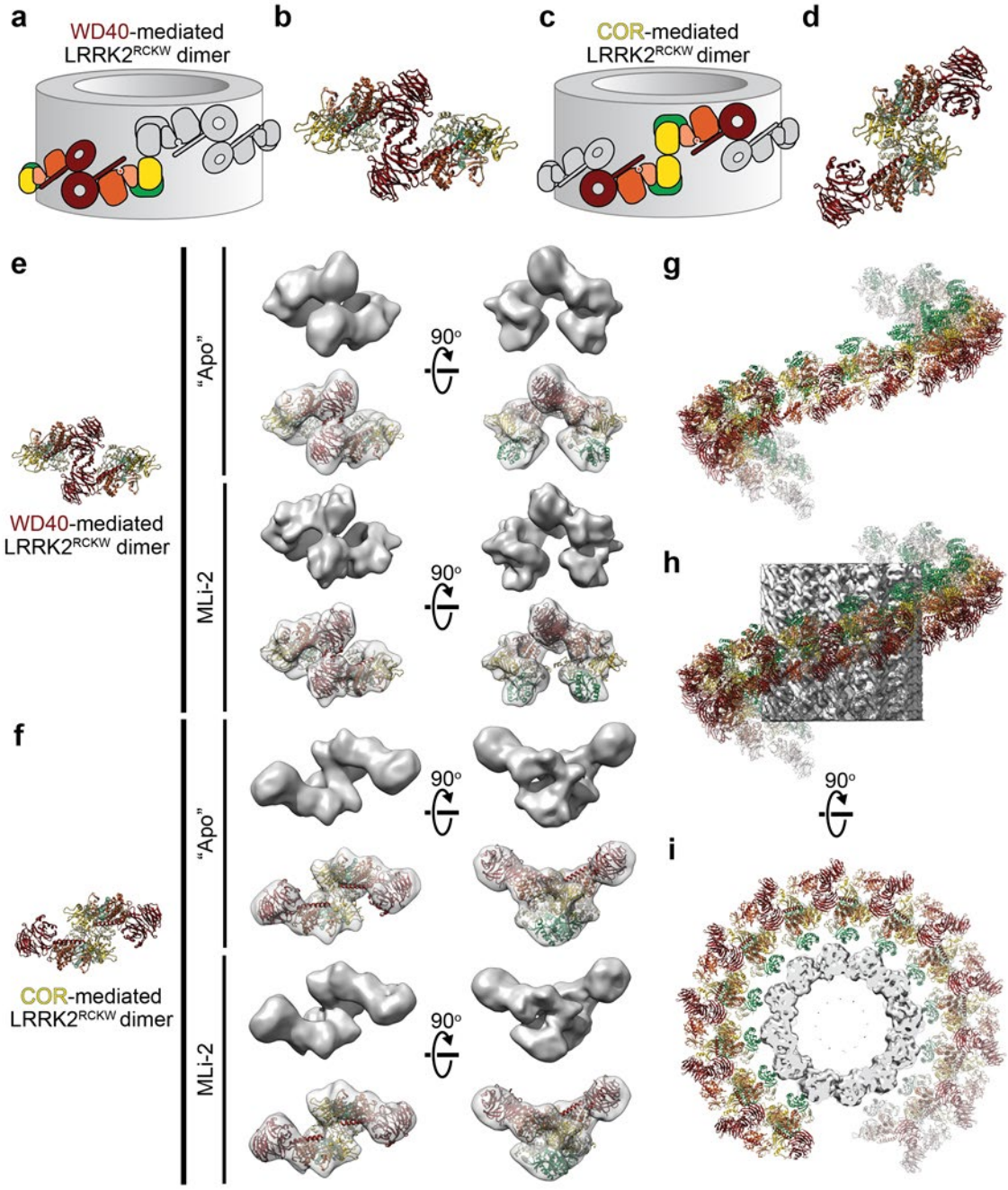
a
WD40-mediated
LRRK2RCKW dimer
b
c
COR-mediated
LRRK2RCKW dimer
d
e
"Apo"
MLi-2
WD40-mediated
LRRK2RCKW dimer
90°
f
"Apo"
MLi-2
COR-mediated
LRRK2RCKW dimer
90°
g
h
90°
i

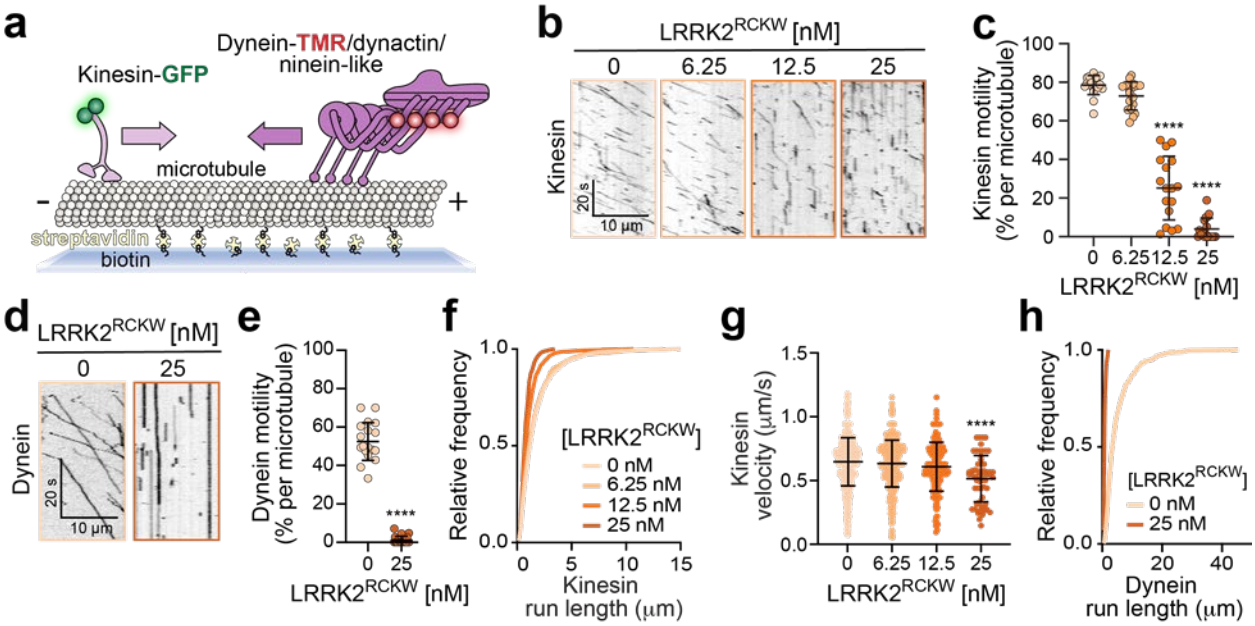

Figure 4 | LRRK2^{RCKW} inhibits the motility of the microtubule-based motors kinesin-1 and cytoplasmic dynein-1. a, Schematic representation of the experimental setup for the single-molecule motility assays. See Methods for details. **b**, Example kymographs showing that increasing concentrations of LRRK2^{RCKW} reduce kinesin-1-GFP (kinesin) runs. **c**, The percentage of motile kinesin events per microtubule as a function of LRRK2^{RCKW} concentration. Data are mean ± s.d. (n = 20, 18, 17, and 18 microtubules from left to right; quantified from two independent experiments). ****p < 0.0001 calculated using the Kruskal-Wallis test with Dunn's posthoc for multiple comparisons. **d**, Example kymographs showing that 25 nM LRRK2^{RCKW} reduces dynein/ dynactin/ ninein-like (dynein) runs. **e**, The percentage of motile dynein events per microtubule as a function of LRRK2^{RCKW} concentration. Data are mean ± s.d. (n = 19 and 21 microtubules from left to right; quantified from two independent experiments). ****p < 0.0001 calculated using the Mann Whitney test. **f**, Cumulative frequency distribution of run lengths of kinesin as a function of LRRK2^{RCKW} concentration. From top to bottom: n = 1166, 1090, 571, and 213 runs. Mean decay constants (tau) ± 95% confidence intervals; microns are 1.667 ± 0.05, 1.570 ± 0.046, 1.048 ± 0.088, and 0.813 ± 0.145. Data quantified from two independent experiments. **g**, Velocity of kinesin as a function of LRRK2^{RCKW} concentration. Data are mean ± s.d. (from left to right: n = 680, 604, 228, and 59 runs quantified from two independent experiments). ****p < 0.0001 calculated using a one-way ANOVA with Dunn's posthoc for multiple comparisons. All other conditions are n.s. **h**, Cumulative frequency distribution of run lengths for dynein as a function of LRRK2^{RCKW} concentration. (n = 659 and 28 runs from top to bottom; mean decay constants (tau) ± 95% confidence intervals; microns are 4.980 ± 0.147 and 0.8460 ± 0.415). Data quantified from two independent experiments. See Extended Data Table 1 for all source data and replicate information.

Figure 5 | Type 2 kinase inhibitors, but not Type 1, rescue microtubule-based motor motility and reduce LRRK2 filament formation in cells. a, Effects of different kinase inhibitors on LRRK2^{RCKW}'s inhibition of kinesin motility. Data is shown as the percentage of motile kinesin events per microtubule as a function of LRRK2^{RCKW} concentration in the absence of any kinase inhibitor (DMSO) or in the presence of the indicated kinase inhibitor (Ponatinib (Type 2): 10 μM; GZD-824 (Type 2): 10 μM; MLi-2 (Type 1): 1 μM; and LRRK2-IN-1 (Type 1): 1 μM). Data are mean ± s.d. (from left to right: n = 34, 17, 30, 18, 14, 23, 10, 12, 14, 14, 14, 8, 12, 11, and 11 microtubules quantified from two to four independent experiments). ****p < 0.0001 calculated using the Kruskal-Wallis test with Dunn's posthoc for multiple comparisons (comparisons were within drug only). **b**, Same as (a) but with dynein/ dynactin/ ninein-like (dynein). DMSO conditions reproduced from Fig. 4c for comparison. (From left to right: n = 19, 21, 9, 18, 13, 16, 7, 8, 14, and 9 microtubules quantified from two independent experiments). ***p < 0.001 and ****p < 0.0001 calculated using the Kruskal-Wallis test with Dunn's posthoc for multiple comparisons (comparisons were within drug only). **c**, The Type 1 kinase inhibitor MLi-2 (500 nM) treated for 2 hrs increases WT GFP-LRRK2 filament formation in 293T cells compared to DMSO-treated control cells. **d**, Quantification of the experiment shown in (c). Data are mean ± s.e.m. (n = 10 [DMSO] and 6 for [MLi-2] technical replicates (~ 20 cells per replicate). ****p=0.0002 Mann Whitney test. **e**, The Type 2 kinase inhibitor GZD-824 (5 μM) treated for 30 mins decreases GFP-LRRK2 (I2020T) filament formation relative to DMSO-treated control cells. **f**, Quantification of the experiment shown in (e). Data are mean ± s.e.m. (n = 9 [DMSO], 8 [5 μM], and 4 [10 μM] technical replicates (> 40 cells per replicate). *p=0.0133 and **p=0.0012 calculated using Krustal-Wallis test with Dunn's posthoc for multiple comparisons. See Extended Data Table 1 for all source data and replicate information. **g**, Schematic representation of our hypothesis that the conformation of LRRK2's kinase controls its association with microtubules. LRRK2 (represented here by LRRK2^{RCKW}) can have its kinase in either an open or closed conformation. The different species we observed (monomers and both COR- and WD40-mediated dimers) are represented in the rounded rectangles, but only monomers are shown on the microtubule for simplicity. Our model proposes that only the kinase-closed form of LRRK2 is compatible with the formation of microtubule-associated filaments. The figure shows a single turn of a LRRK2 filament to emphasize that we propose that shorter species will be the relevant ones under physiological conditions. The two interfaces that mediate filament formation, which are the same ones observed in the dimers, are indicated.

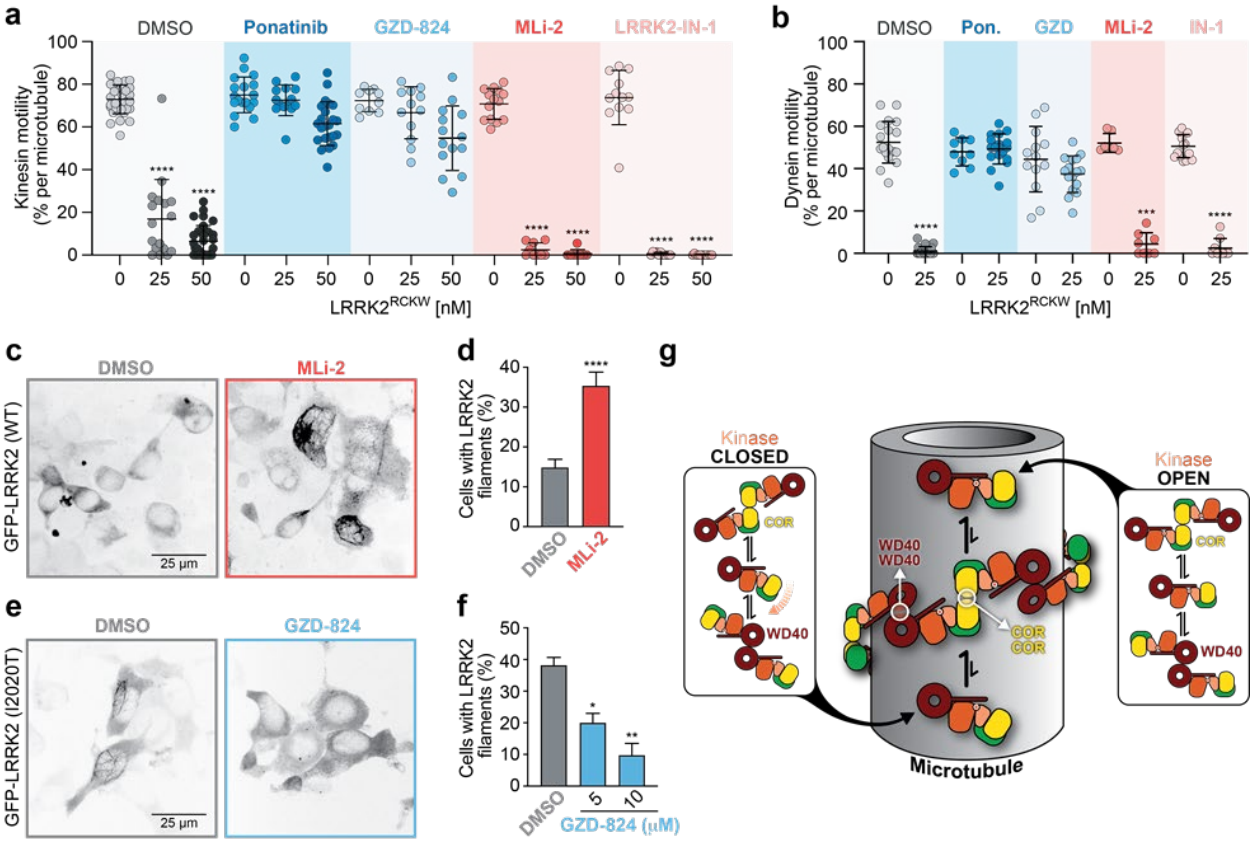
a
DMSO
Ponatinib
GZD-824
MLi-2
LRRK2-IN-1
Kinesin motility (% per microtubule)
LRRK2RCKW [nM]
b
DMSO
Pon.
GZD
MLi-2
IN-1
Dynein motility (% per microtubule)
LRRK2RCKW [nM]
c
DMSO
MLi-2
GFP-LRRK2 (WT)
25 µm
d
Cells with LRRK2 filaments (%)
DMSO
MLi-2
e
DMSO
GZD-824
GFP-LRRK2 (I2020T)
25 µm
f
Cells with LRRK2 filaments (%)
DMSO
GZD-824 (µM)
g
Kinase CLOSED
COR
WD40
Kinase OPEN
WD40 WD40
COR COR
Microtubule

EXTENDED DATA FIGURES

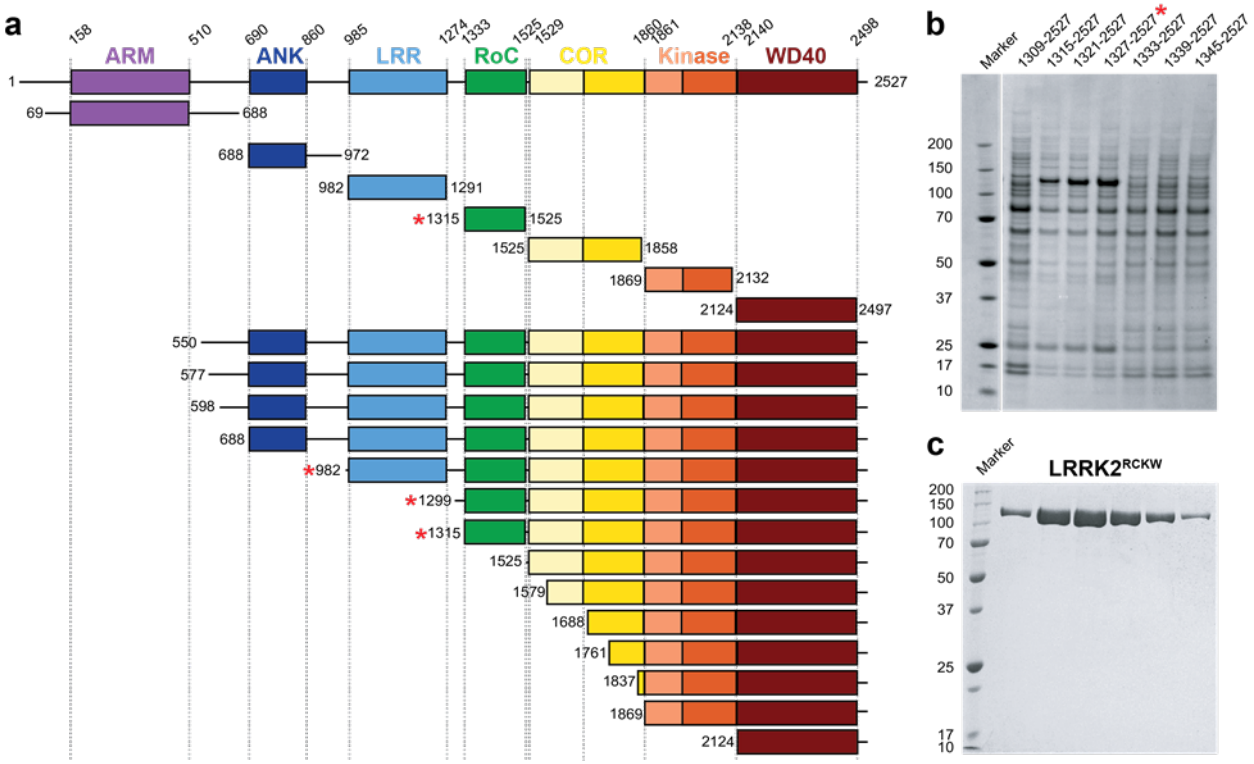

Extended Data Figure 1 | Optimization of LRRK2 constructs for expression in insect cells. **a**, We systematically scanned domain boundaries (amino acid numbers of boundaries noted above domain names) to generate LRRK2 constructs that expressed well in baculovirus-infected insect cells and yielded stable and soluble protein. These attempts included full-length LRRK2, the kinase domain alone or with the WD40 domain, and other isolated domains. In this approach, only the GTPase domain on its own expressed well. Next, we gradually shortened LRRK2 from its amino terminus. Red asterisks indicate constructs that were soluble. **b**, After identifying domain boundaries yielding constructs that expressed soluble protein, additional fine tuning of boundaries was performed. A Coomassie stained SDS-PAGE gel shows systematic N-terminal truncations at the RoC domain resulting in the identification of a construct with the highest expression levels: amino acids 1327 to 2527 (red asterisk, "LRRK2^{RCKW}" here). **c**, A Coomassie stained SDS-PAGE gel of purified LRRK2^{RCKW} after elution from an S200 gel filtration column. As predicted by its primary structure, LRRK2^{RCKW} runs at ~140 kDa.

Extended Data Figure 2 | Cryo-EM structure determination of LRRK2^{RCKW}. a, Electron micrograph of LRRK2^{RCKW}. **b**, 2D class averages of the LRRK2^{RCKW} trimer. **c**, 2D/3D classification scheme used to obtain the 3.5Å structure of the LRRK2^{RCKW} trimer. **d**, **e**, Fourier Shell Correlations (from Cryosparc) (d) and Euler angle distribution (e) for the LRRK2^{RCKW} trimer. **f**, Processing strategy used to obtain a 3.8Å structure of LRRK2^{RCKW} generated from a signal-subtracted trimer where only one monomer contains the RoC and COR-A domains. This structure improved the resolution of the RoC and COR-A domains relative to the trimer shown in (c). **g-i**, 2D class averages (g), Fourier Shell Correlations (from Relion) (h), and Euler angle distribution (from Relion) (i) for the 3.8Å-resolution signal-subtracted LRRK2^{RCKW} structure. **j**, Close-ups of different parts of the final structure, with the 3.8Å map as a semi-transparent surface and the model shown using the coloring scheme introduced in Fig. 1a.

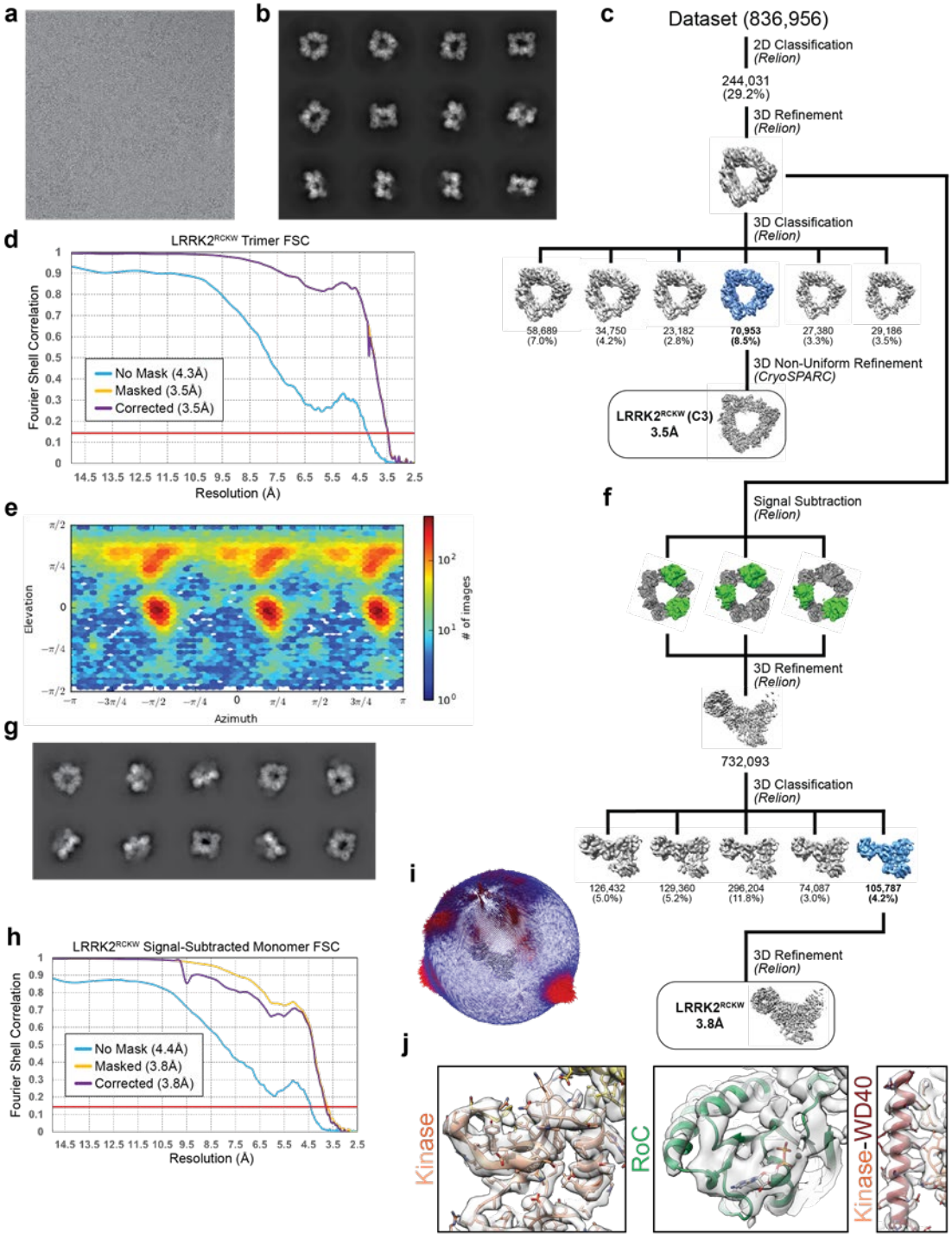
a
b
c
Dataset (836,956)
2D Classification
(Relion)
244,031
(29.2%)
3D Refinement
(Relion)
3D Classification
(Relion)
58,689
(7.0%)
34,750
(4.2%)
23,182
(2.8%)
70,953
(8.5%)
27,380
(3.3%)
29,186
(3.5%)
3D Non-Uniform Refinement
(CryoSPARC)
LRRK2RCKW (C3)
3.5Å
d
LRRK2RCKW Trimer FSC
Fourier Shell Correlation
No Mask (4.3Å)
Masked (3.5Å)
Corrected (3.5Å)
Resolution (Å)
e
Elevation
Azimuth
# of images
f
Signal Subtraction
(Relion)
3D Refinement
(Relion)
732,093
3D Classification
(Relion)
126,432
(5.0%)
129,360
(5.2%)
296,204
(11.8%)
74,087
(3.0%)
105,787
(4.2%)
3D Refinement
(Relion)
LRRK2RCKW
3.8Å
g
h
LRRK2RCKW Signal-Subtracted Monomer FSC
Fourier Shell Correlation
No Mask (4.4Å)
Masked (3.8Å)
Corrected (3.8Å)
Resolution (Å)
i
j
Kinase
RoC
Kinase-WD40

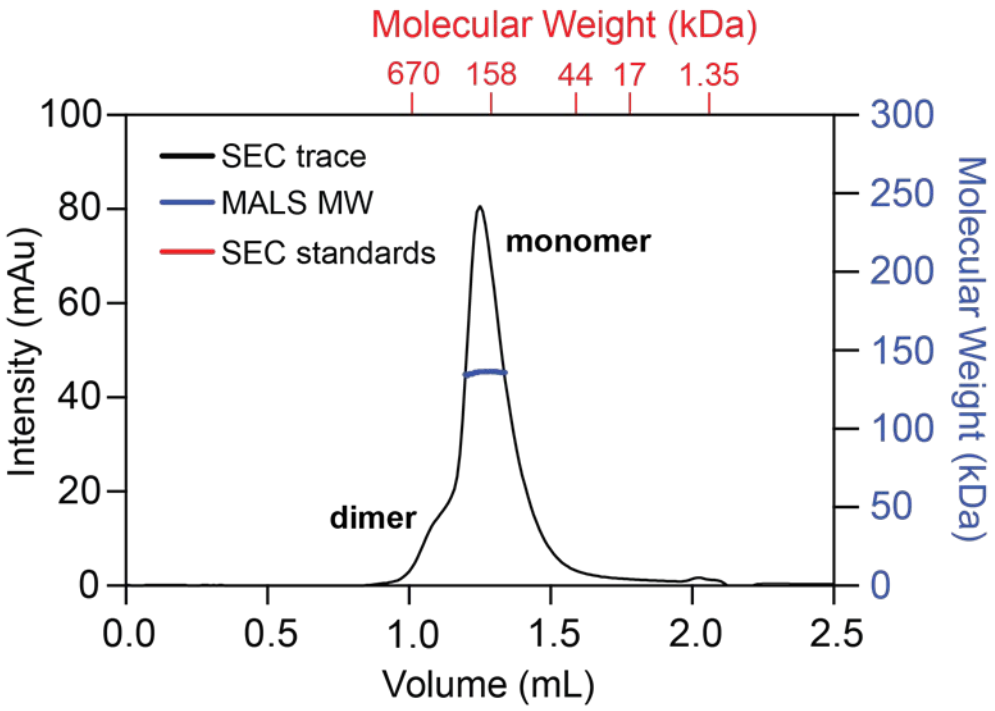

MW	SEC	MALS
137.9kDa	227kDa	136kDa

Extended Data Figure 3 | LRRK2^{RCKW} is predominantly a monomer under the conditions used for cryo-EM. Size Exclusion Chromatography-Multiple Angle Light Scattering (SEC-MALS) analysis of LRRK2^{RCKW} under the conditions used for cryo-EM (Fig. 1). The table below the elution profile shows the calculated molecular weights (MW) of LRRK2^{RCKW} according to SEC standards ("SEC") and MALS.

Extended Data Figure 4 | Comparisons between LRRK2 and other kinases. a, View of the LRRK2^{RCKW} atomic model with COR-A, COR-B and kinase domains colored. The N- and C-lobes of the kinase are labeled, as is the αC helix in the N-lobe. **b**, **c**, The FAK-FERM (PDB: 2J0J) [27] (b) and CDK2-Cyclin A (PDB: 2CCH) [29] (c) complexes, shown in the same orientation as the kinase in (a). The αC helix of CDK2 is also labeled. **d**, Same view as in (a) with only the kinase domain and the C-terminal helix colored. **e**, Rotated view of LRRK2's kinase domain with the C-terminal helix facing the viewer. **f**, **g**, CDKL3 (PDB: 3ZDU) (f) and RIPK2 (PDB: 4C8B) [35] (g) shown in the same orientation as LRRK2's kinase in (e), with alpha helices with the same general location as LRRK2's C-terminal helix colored in green. **h**, KSR2-MEK1 complex (PDB: 2Y4I), with the kinase oriented as in (e) (left) and after removing KSR2 for clarity (right). The alpha helix associated with the kinase is shown in green. **i**, HCK (PDB: 2HCK) in complex with its SH2 and SH3 domains with the kinase oriented as in (e) (left), and after removal of the SH2 and SH3 domains for clarity (right). A remaining alpha helix from the SH2 domain is shown in yellow. **j**, Front view of LRRK2's kinase with the C-Spine and R-Spine residues shown and colored in grey and white, respectively. **k**, Close-up of the DYG motif and neighboring R-Spine residues.

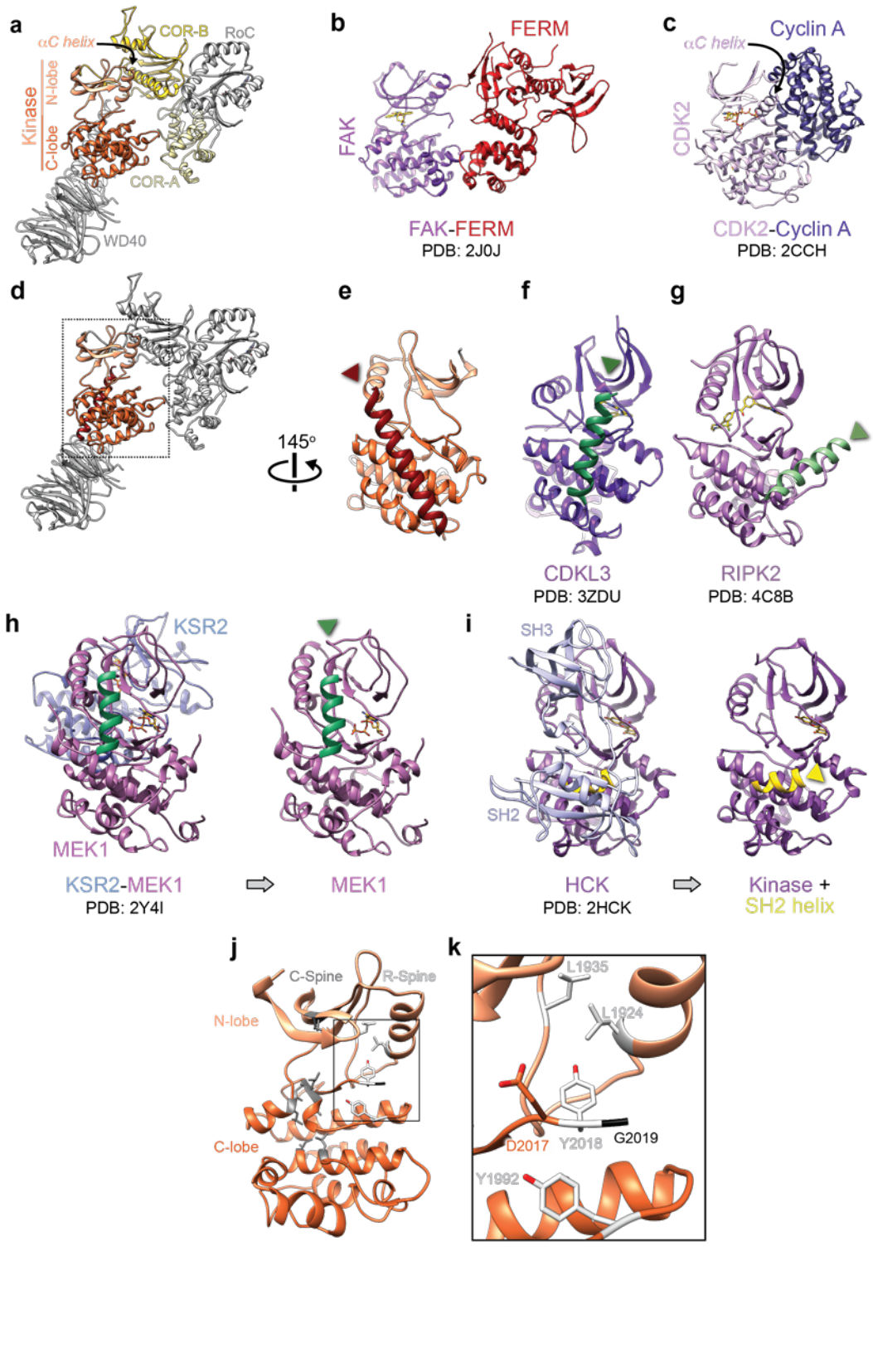
a
αC helix
COR-B
RoC
Kinase
N-lobe
C-lobe
COR-A
WD40
b
FERM
FAK
FAK-FERM
PDB: 2J0J
c
αC helix
Cyclin A
CDK2
CDK2-Cyclin A
PDB: 2CCH
d
145°
e
f
CDKL3
PDB: 3ZDU
g
RIPK2
PDB: 4C8B
h
KSR2
MEK1
KSR2-MEK1
PDB: 2Y4I
MEK1
i
SH3
SH2
HCK
PDB: 2HCK
Kinase +
SH2 helix
j
C-Spine
R-Spine
N-lobe
C-lobe
k
L1935
L1924
D2017
Y2018
G2019
Y1992

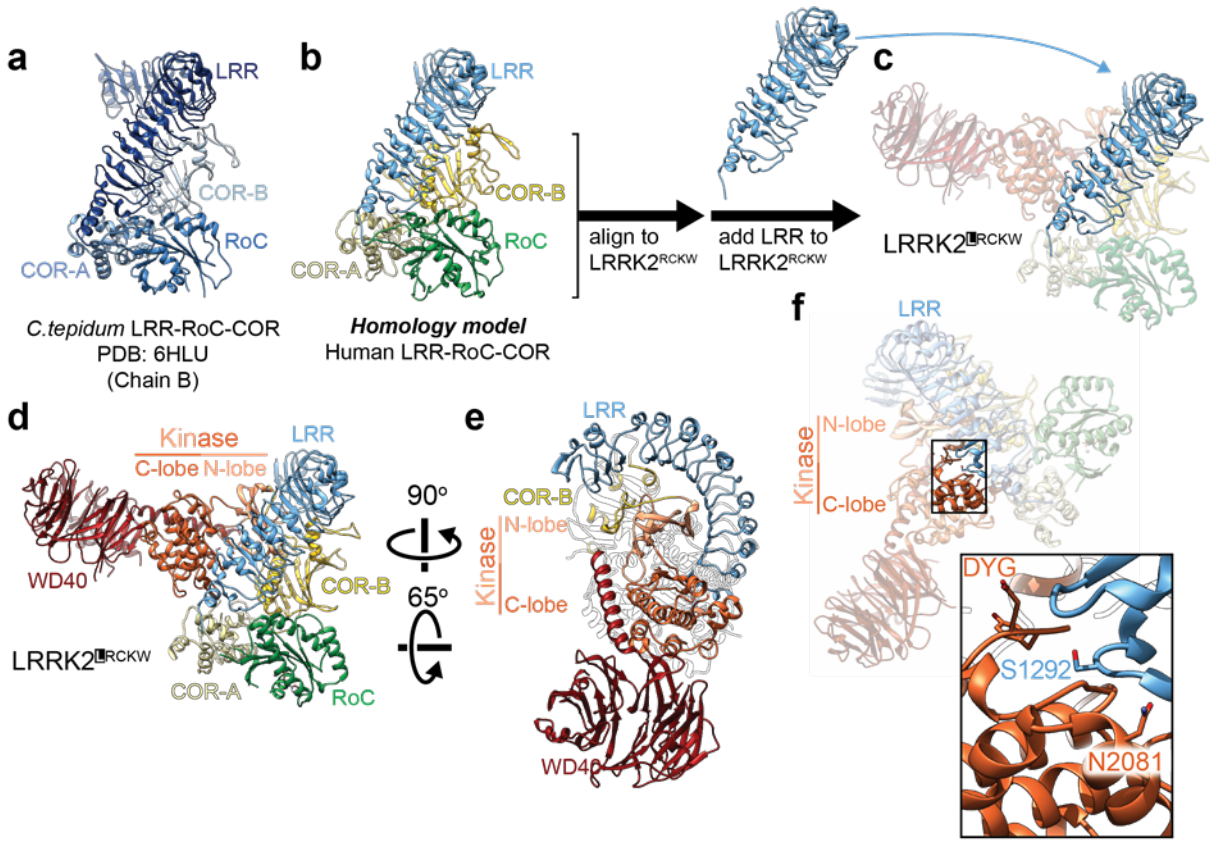

Extended Data Figure 5 | Modelling of the Leucine-Rich Repeat (LRR) into LRRK2^{RCKW}. a, Crystal structure of the LRR-RoC-COR(A/B) domains from C. tepidum Roco (PDB: 6HLU) [15]. **b**, Homology model for human LRR-RoC-COR(A/B) based on the C. tepidum Roco structure (from SWISS-MODEL). **c**, Chimeric model combining LRRK2^{RCKW} and the homology model for the LRR domain from (b) obtained by aligning their RoC-COR(A/B) domains. **d**, **e**, Two views of the hybrid LRRK2^{LRCKW} model. **f**, Close-up showing the proximity between the active site of the kinase (with the side chains of its DYG motif shown) and the S1292 autophosphorylation site on the LRR. The close-up also highlights the proximity between N2081, a residue implicated in Crohn's Disease, and the LRR.

Extended Data Figure 6 | Docking of LRRK2^{RCKW} into the sub-tomogram average of cellular LRRK2 filaments, and modeling of the closed-kinase LRRK2^{RCKW} filaments. a, The WD40s in the crystal structure of a dimer of LRRK2's WD40 (PDB: 6DLP)[18] were replaced with the WD40s from our cryo-EM structure of LRRK2^{RCKW}. **b**, The resulting dimer was fitted into the 14Å sub-tomogram average of cellular microtubule-associated LRRK2 filaments. **c**, Two views of the same fitting shown in (b), displayed with a higher threshold for the map to highlight the fitting of the WD40 β-propellers into the density. **d**, Four copies of LRRK2^{RCKW} were docked into the sub-tomogram average by aligning their WD40 domains to the docked WD40 dimer. **e**, Model containing the four aligned LRRK2^{RCKW}. **f-i**, Modeling of the kinase-closed form of LRRK2^{RCKW}. **f**, **g**, The structure of ITK bound to an inhibitor (PDB: 3QGY)[54], which is in a closed conformation, was aligned to LRRK2^{RCKW} using only the C-lobes of the two kinases. **h**, The N-terminal portion of LRRK2^{RCKW}, comprising RoC, COR-A, COR-B and the N-lobe of the kinase, was aligned to ITK using only the N-lobes of the kinases. RoC, COR-A and COR-B were moved as a rigid body in this alignment. **i**, A kinase-closed model of LRRK2^{RCKW}. **j**, Superposition of the kinase-open (our cryo-EM structure) and kinase-closed LRRK2^{RCKW} (the model built here, in blue) showing the closing of the RoC-COR(A/B)-kinase N-lobe portion of LRRK2^{RCKW}. Three structural reference points are shown in colors and numbered to highlight the differences between the two structures.

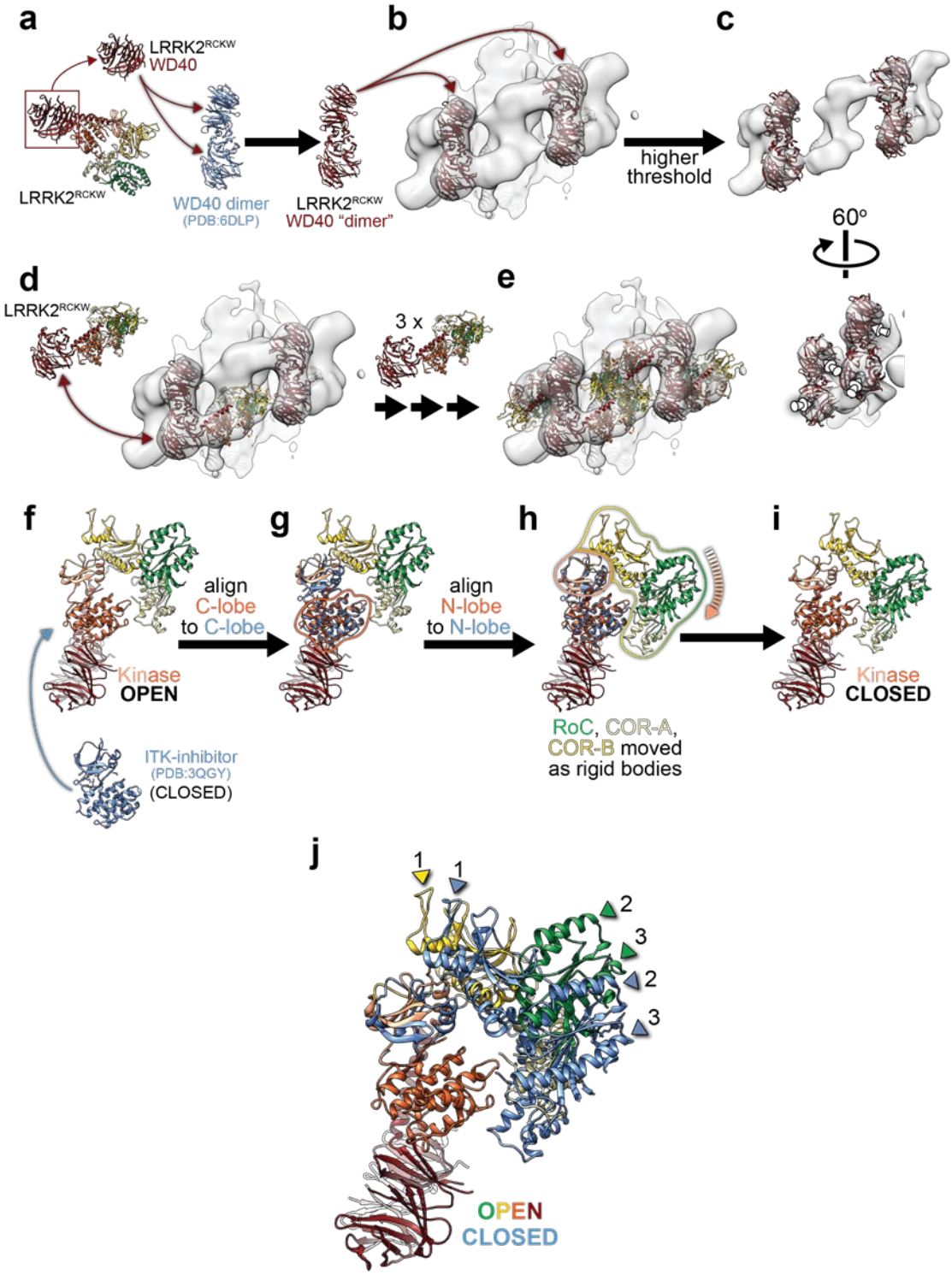
a
LRRK2RCKW WD40
LRRK2RCKW
WD40 dimer (PDB:6DLP)
LRRK2RCKW WD40 "dimer"
b
higher threshold
c
60°
d
LRRK2RCKW
3 x
e
f
align C-lobe to C-lobe
Kinase OPEN
ITK-inhibitor (PDB:3QGY) (CLOSED)
g
align N-lobe to N-lobe
h
RoC, COR-A, COR-B moved as rigid bodies
i
Kinase CLOSED
j
1
1
2
3
2
3
OPEN
CLOSED

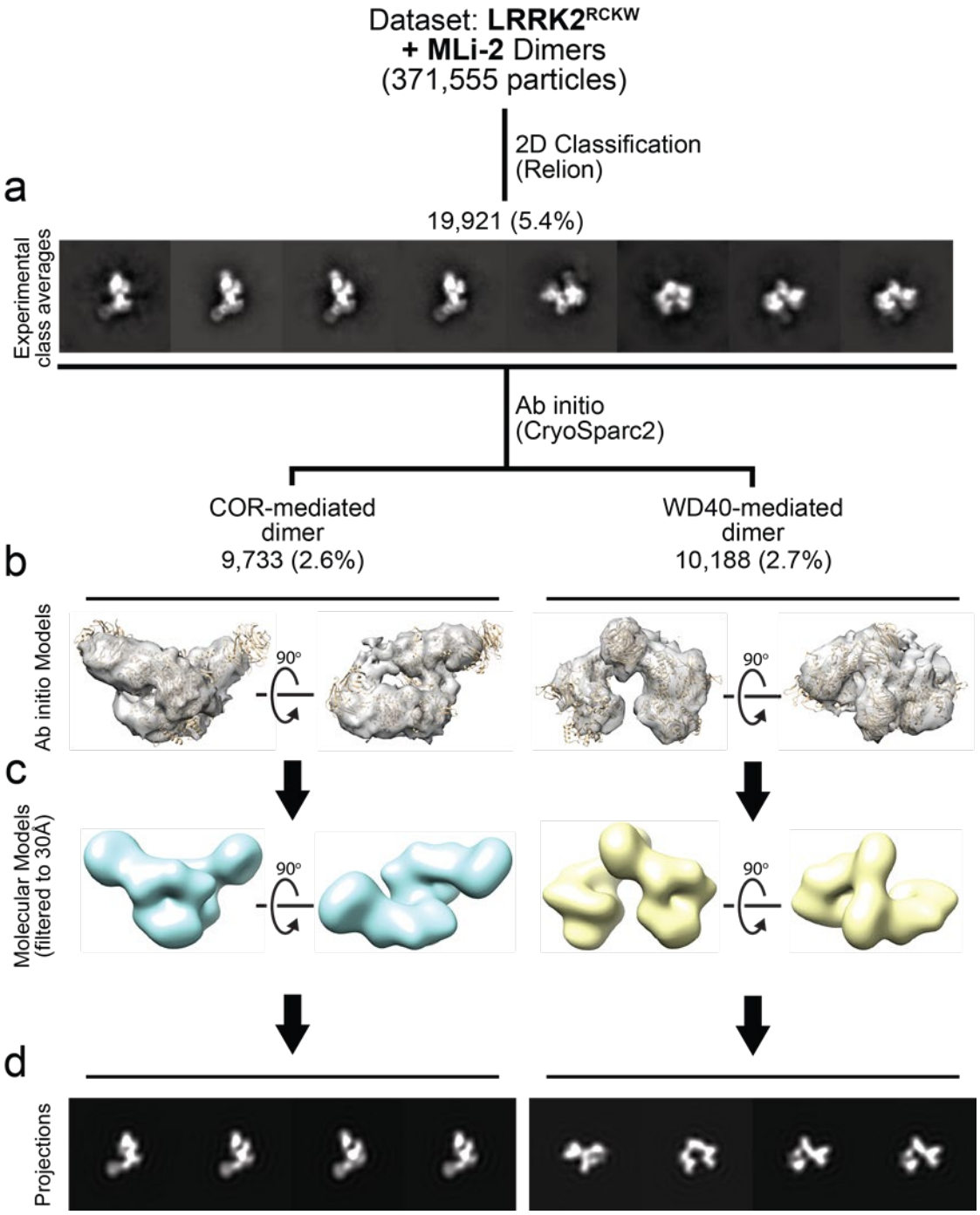

Extended Data Figure 7 | Generation of ab initio models for cryo-EM of LRRK2^{RCKW} dimers. An initial dataset was collected from a sample of LRRK2^{RCKW} incubated in the presence of the kinase inhibitor MLi-2 and dimers were selected. a, Representative two-dimensional class averages used for ab initio model building. **b**, Ab initio models with the structure of LRRK2^{RCKW} docked in. **c**, Volumes generated form the molecular models in (b), filtered to 30Å resolution. **d**, Projections of the volumes in (c) shown in the same order as their corresponding 2D class averages in (a).

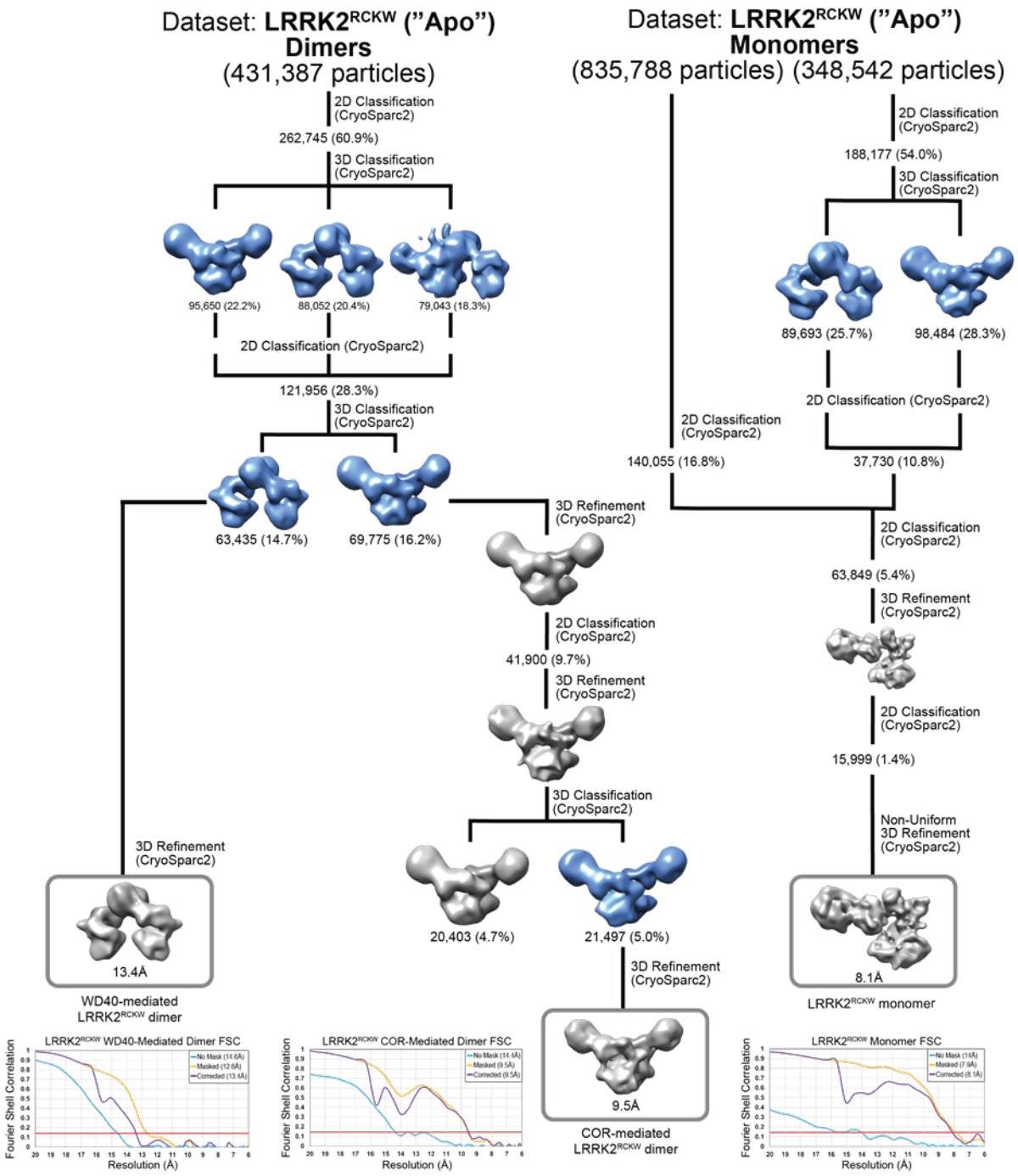

Extended Data Figure 8 | Data processing strategy for obtaining cryo-EM structures of a monomer and WD40- and COR-mediated dimers of LRRK2^{RCKW} in the absence of inhibitor ("Apo"). The models used during the processing of the dimers (see Methods) are those shown in Extended Data Fig. 7 along with an additional linear trimer (see Methods) used for particle sorting. The models used for processing of the monomer (see Methods) were the same dimer models as in Extended Data Fig. 7 (used for particle sorting) in addition to a monomer model generated from our LRRK2^{RCKW} model (used for refinement).

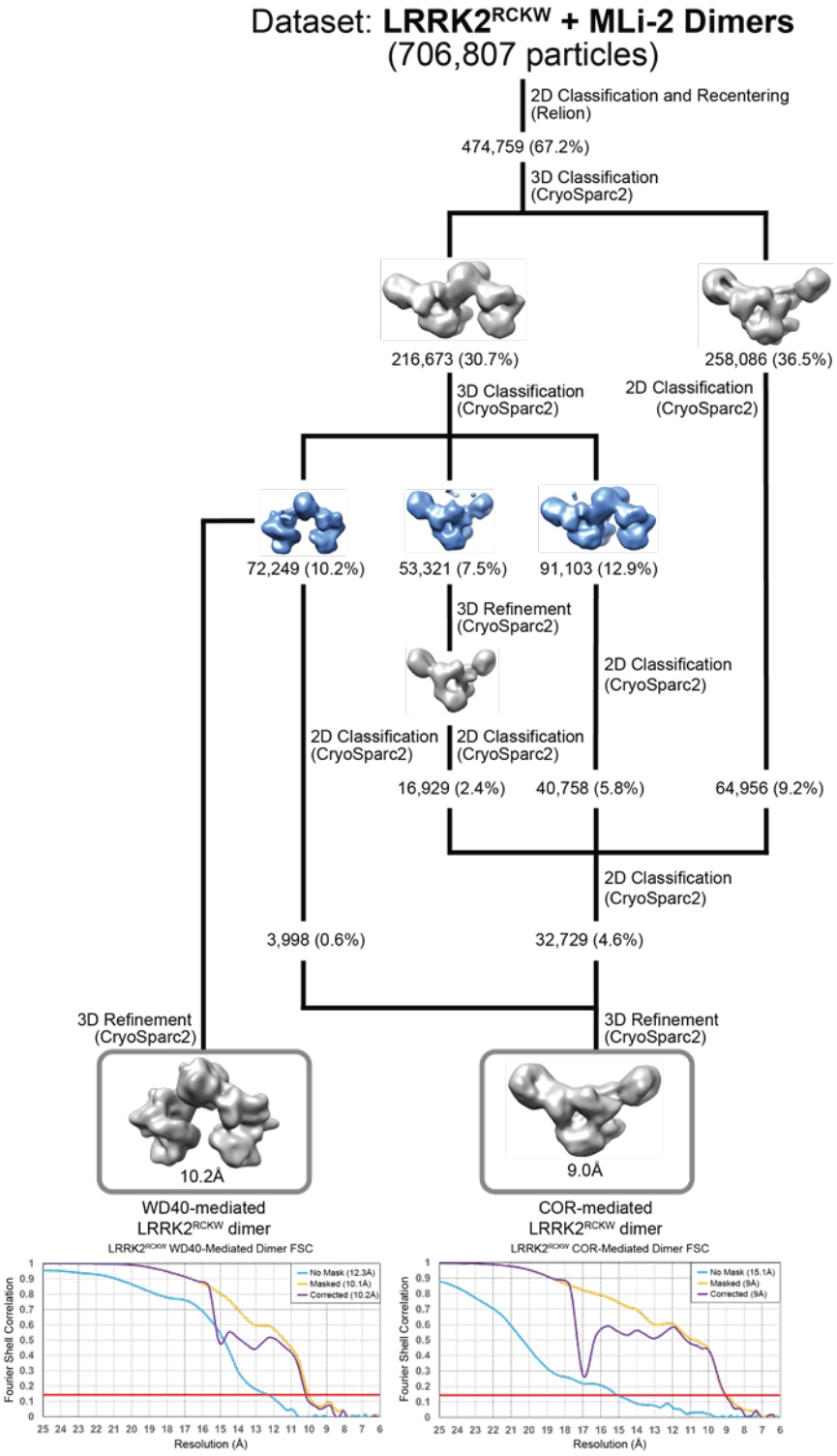

Extended Data Figure 9 | Data processing strategy for obtaining cryo-EM structures of WD40- and COR-mediated dimers of LRRK2^{RCKW} in the presence of the inhibitor MLi-2. The models used during this processing (see Methods) are those shown in Extended Data Fig.7 along with an additional linear trimer (see Methods) used for particle sorting.

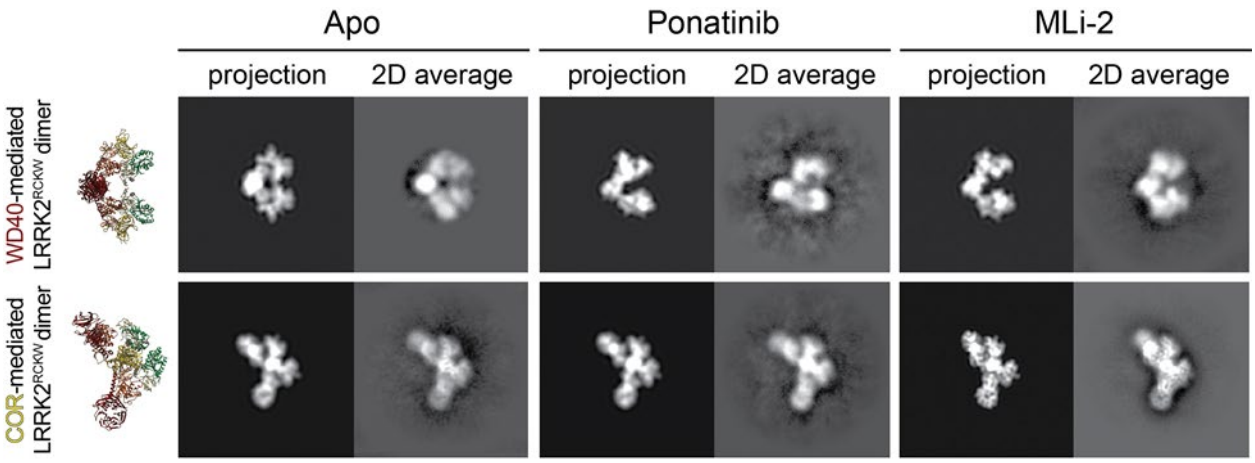

Extended Data Figure 10 | LRRK2^{RCKW} forms WD40- and COR-mediated dimers outside the filaments. Two-dimensional (2D) class averages of WD40- and COR-mediated LRRK2^{RCKW} dimers obtained in the absence of inhibitors ("Apo") or in the presence of either Ponatinib or MLi-2. The same molecular models of the two dimers shown in Fig. 3 are shown on the left but in orientations similar to those represented by the 2D class averages shown here. For each class average, a projection from the corresponding model in the best-matching orientation is shown to its left.

Extended Data Figure 11 | The basic geometric properties of the microtubule-associated LRRK2^{RCKW} filaments are encoded in the structure of LRRK2^{RCKW}. a, **b**, The LRRK2^{RCKW} structure solved in this work (a) was split at the junction between the N- and C-lobes of the kinase domain (L1949-A1950) (b). **c**, **d**, Docking of the two halves of LRRK2^{RCKW} into cryo-EM maps of LRRK2^{RCKW} solved in the presence of MLi-2 (c) or without inhibitor ("Apo") (d). The dimer maps are the same ones shown in Fig. 3 and Extended Data Figs. 8 and 9 and the Apo map is the one shown in Fig. 1g, h and Extended Data Fig. 8. **e**, Three-way comparison of LRRK2^{RCKW} (with domain colors) and the models resulting from the dockings into the MLi-2 WD40-mediated dimer map (c) (dark blue) and "Apo" monomer map (d) (light blue). The three structures were aligned using the C-lobes of their kinases and the WD40 domain. The superposition illustrates that the docking into the "Apo" map results in a structure very similar to that obtained from the trimer (Fig. 1) and that the presence of MLi-2 leads to a closing of the kinase. **f**, The model obtained in (c) was docked into cryo-EM maps of either WD40- or COR-mediated dimers obtained in the presence of MLi-2. **g**, Molecular models resulting from the docking in (f). **h**, Aligning, in alternating order, copies of the dimer models generated in (f, g) results in a right-handed filament with dimensions compatible with those of a microtubule, and its RoC domains pointing inwards (see Fig. 3g-i for more details).

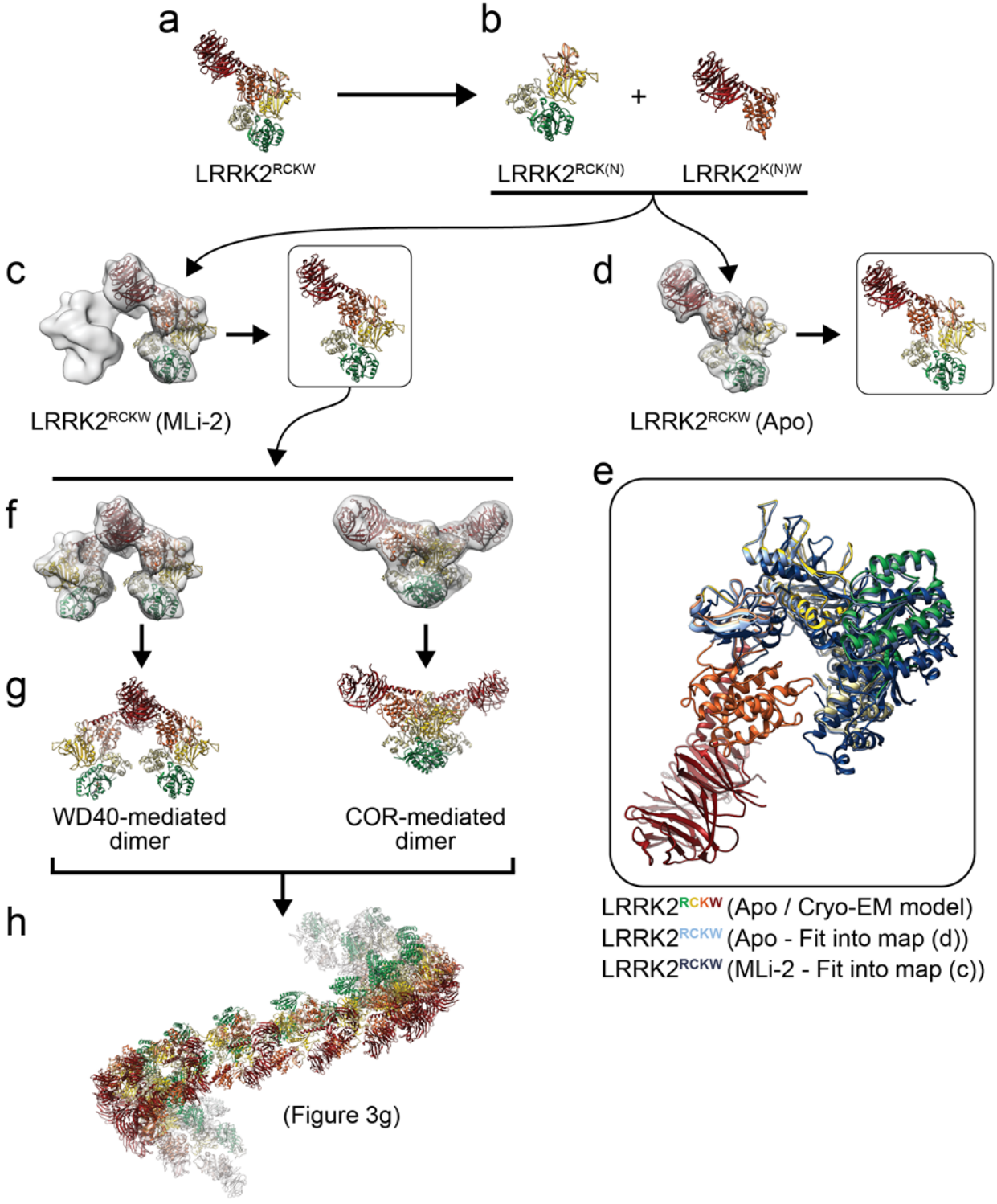
a
b
LRRK2RCKW
LRRK2RCK(N)
LRRK2K(N)W
c
d
LRRK2RCKW (MLi-2)
LRRK2RCKW (Apo)
e
f
g
WD40-mediated dimer
COR-mediated dimer
h
(Figure 3g)
LRRK2RCKW (Apo / Cryo-EM model)
LRRK2RCKW (Apo - Fit into map (d))
LRRK2RCKW (MLi-2 - Fit into map (c))

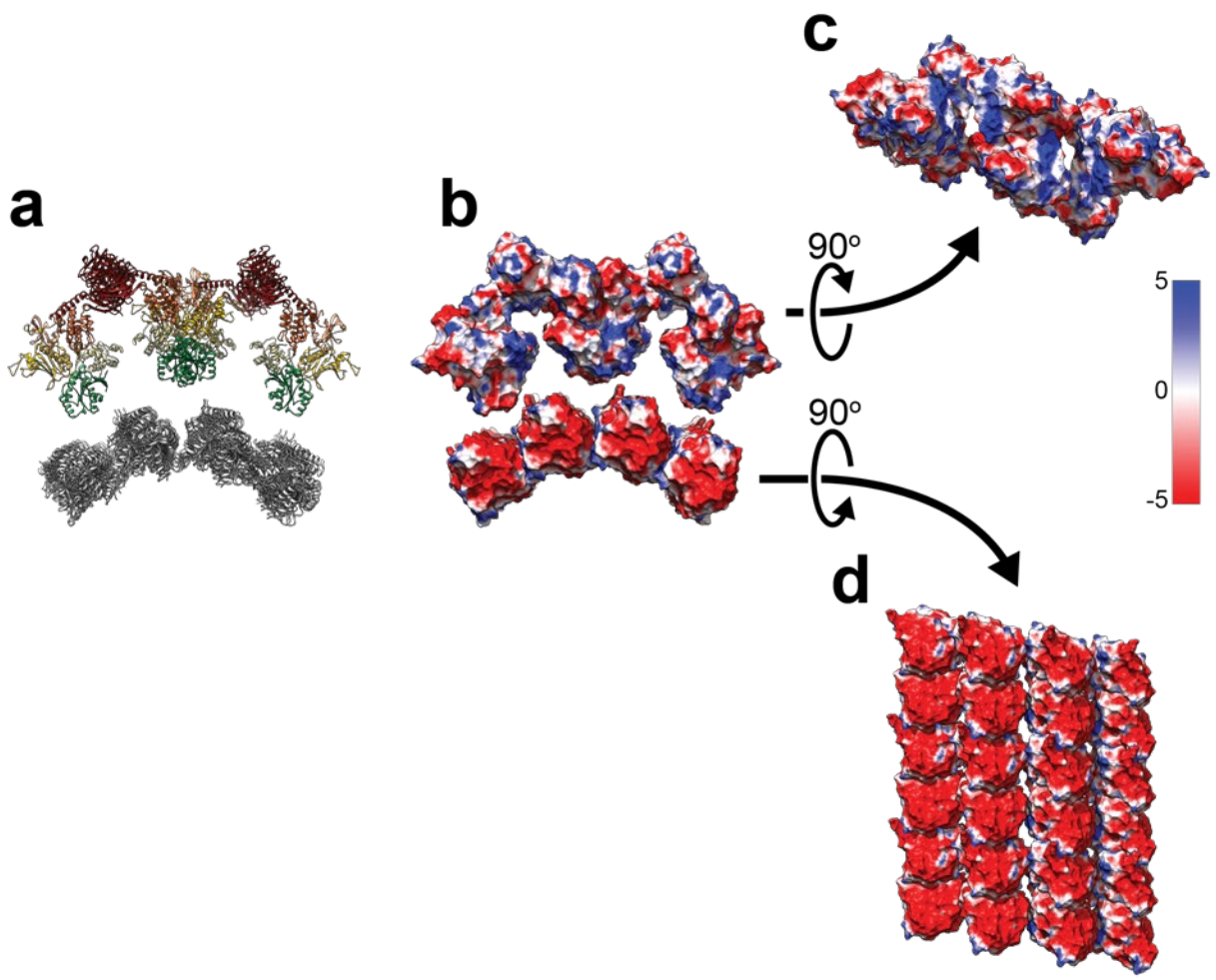

Extended Data Figure 12 | Complementarity between the surface charge distributions of the LRRK2^{RCKW} filament model and the microtubule. a, Molecular model of the microtubule-associated LRRK2^{RCKW} filament obtained by docking a fragment of a microtubule structure (PDB: 6O2S) into the corresponding density in the sub-tomogram average (Fig. 2a). **b**, Same view as in (a) with the models shown as surface representations colored by their Coulomb potential. **c**, **d**, "Peeling off" of the structure shown in (b), with the LRRK2^{RCKW} filament seen from the perspective of the microtubule surface (c) and the microtubule surface seen from the perspective of the LRRK2^{RCKW} filament (d). Note: the acidic C-terminal tubulin tails are not ordered in the microtubule structure and thus are not included in the surface charge distributions. The Coulomb potential coloring scale is shown on the right.

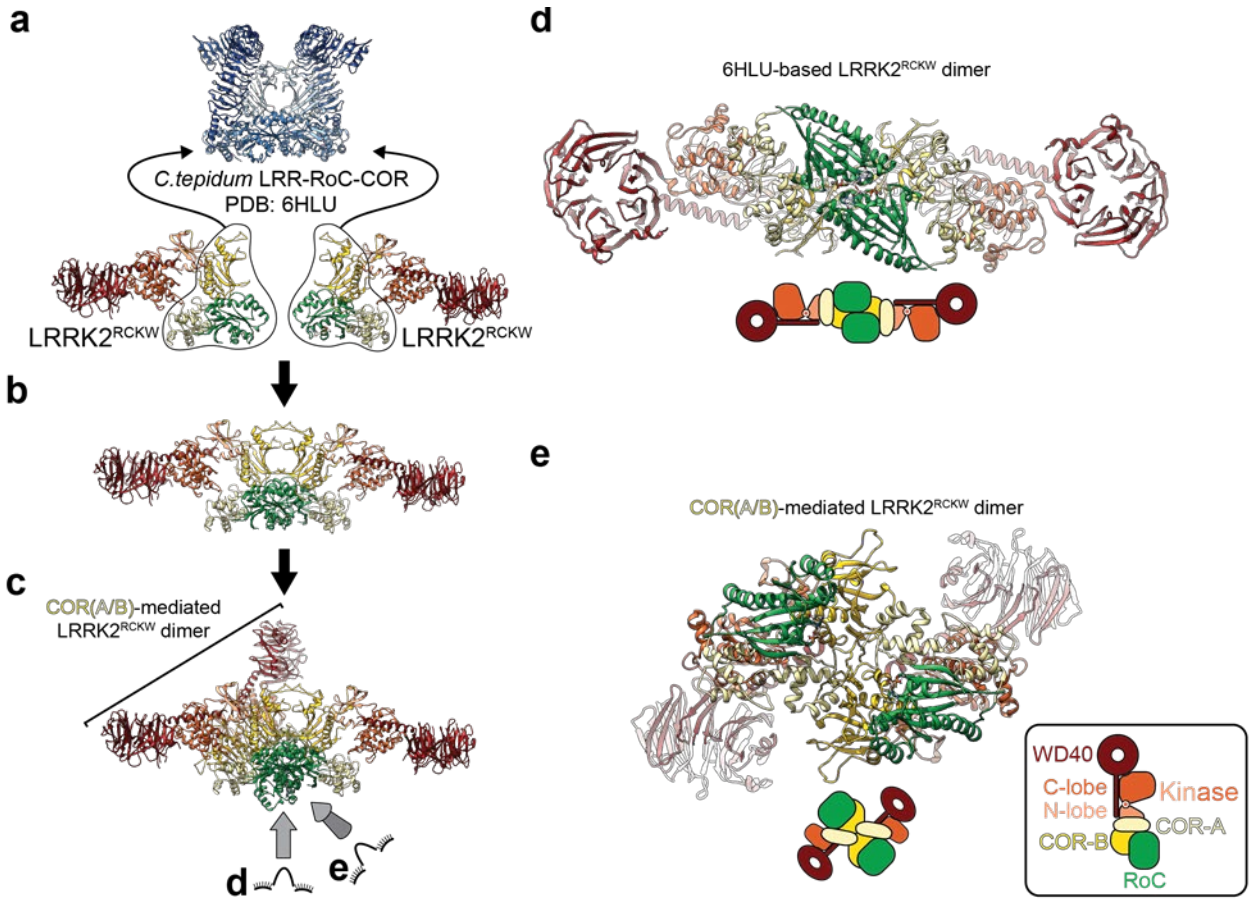

Extended Data Figure 13 | LRRK2^{RCKW}'s COR-mediated dimerization interface differs from that of the C. tepidum's Roco homolog. a, **b**, Two copies of the LRRK2^{RCKW} structure were aligned to the RoC-COR domains of the LRR-RoC-COR structure from C. tepidum's Roco protein (PDB: 6HLU) (a) to replicate the interface observed in the bacterial homolog in the context of the human protein (b). **c**, One of the LRRK2^{RCKW} monomers was used to superimpose the dimer modeled in (b) with the COR-mediated dimer seen both in the microtubule-associated filaments in cells (cryo-ET) (Fig. 2) as well as in the absence of microtubules (by cryo-EM) (Fig. 3). **d**, **e**, Comparison between the dimer modeled based on the C. tepidum LRR-RoC-COR structure (d) and the dimer observed for LRRK2^{RCKW} in this work (e). While the bacterial structure shows a dimerization interface that involves the GTPase (RoC), LRRK2^{RCKW} interacts exclusively through its COR-A and -B domains, with the RoC domains located away from this interface. The two arrangements are shown schematically in cartoon form below the structures.

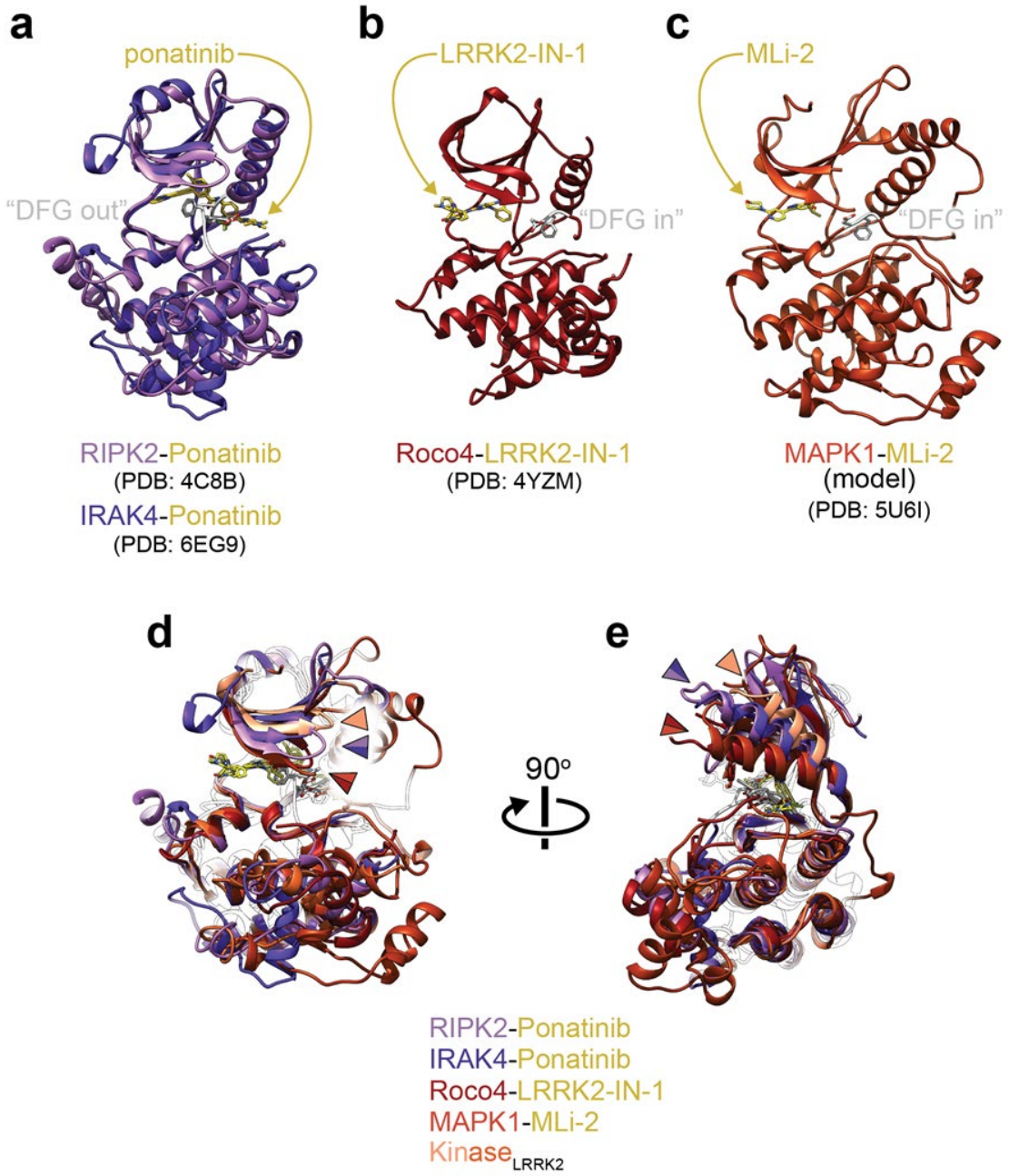

Extended Data Figure 14 | Ponatinib is a Type 2, "DFG out" inhibitor. a, Superposition of the structures of Ponatinib-bound RIPK2 (PDB: 4C8B) [55] and IRAK4 (PDB: 6EG9). Ponatinib is shown in yellow, and the DYG motif residues are shown in white. **b**, **c**, For comparison, the structures of (a) Roco4 bound to LRRK2-IN-1 (PDB: 4YZM), a LRRK2-specific Type 1, "DFG in" inhibitor, and (b) a model of Mitogen-activated kinase 1 (MAPK1) bound to MLi-2 (PDB: 5U6I), another LRRK2-specific Type 1, "DFG in" inhibitor are shown. The inhibitor and DFG residues are colored as in (a). **d**, The structures in (a-c), as well as the kinase from $LRRK2^{RCKW}$ are shown superimposed. The color arrowheads point to the N-lobe's β-sheet to highlight the difference in conformation between kinases bound to the two different types of inhibitors. Note that $LRRK2^{RCKW}$'s kinase is even more open than the two Ponatinib-bound kinases. **e**, Rotated view of (d), now highlighting the position of the N-lobe's αC helix. An additional alpha helix in the N-lobe of MAPK1 was removed from this view for clarity.

Extended Data Figure 15 | Type 2 kinase inhibitors rescue microtubule-based motor motility. a, The kinase inhibitors MLi-2 (1 μM), LRRK2-IN-1 (1 μM), Ponatinib (10 μM) and GZD-824 (10 μM) all inhibit LRRK2^{RCKW}'s kinase activity *in vitro* compared to a DMSO control. A Western blot using a phospho-specific antibody to Rab8a at the indicated time points is shown. **b**, A dose response curve showing the percentage of motile kinesin events per microtubule as a function of Ponatinib concentration with LRRK2^{RCKW} (25 nM) or without LRRK2^{RCKW}. Data are mean ± s.d. (from left to right: n = 12, 18, 16, 14, and 9 microtubules quantified from one experiment). ****p < 0.0001 calculated using the Kruskal-Wallis test with Dunn's posthoc for multiple comparisons (compared to DMSO without LRRK2^{RCKW}). **c**, Dose response curve of run lengths from data in (b) represented as a cumulative frequency distribution. From top to bottom: n = 654, 173, 584, 293, and 129 motile kinesin events. Mean decay constants (tau) ± confidence interval (CI) are (from top to bottom) 2.736 ± 0.113, 1.291 ± 0.181, 2.542 ± 0.124, 2.285 ± 0.134, and 1.653 ± 0.17. **d**, Representative kymographs of kinesin and dynein with DMSO or Type 2 inhibitors with or without LRRK2^{RCKW}. **e**, The Type 2 kinase inhibitors Ponatinib and GZD-824 rescue kinesin run length, represented as a cumulative frequency distribution of run lengths with LRRK2^{RCKW} (25 nM) or without LRRK2^{RCKW} (0 nM). From top to bottom: n = 893, 355, 507, 499, 524, and 529 runs from two independent experiments. Mean decay constants (tau) ± 95% CI are (from top to bottom) 2.070 ± 0.058, 0.8466 ± 0.091, 1.938 ± 0.065, 2.075 ± 0.07, 1.898 ±, 0.065, and 1.718 ± 0.064. **f**, Same as in (e) but with dynein. From top to bottom: n = 659, 28, 289, 306, 254, and 339 runs from two independent experiments). Mean decay constants (tau) ± 95% confidence intervals; microns are 4.980 ± 0.147, 0.846 ± 0.415, 4.686 ± 0.142, 4.445 ± 0.172, 3.156 ± 0.09, 3.432 ± 0.188 (from top to bottom). The DMSO conditions are reproduced from Fig. 4f for comparison. See Extended Data Table 1 for all source data and replicate information.

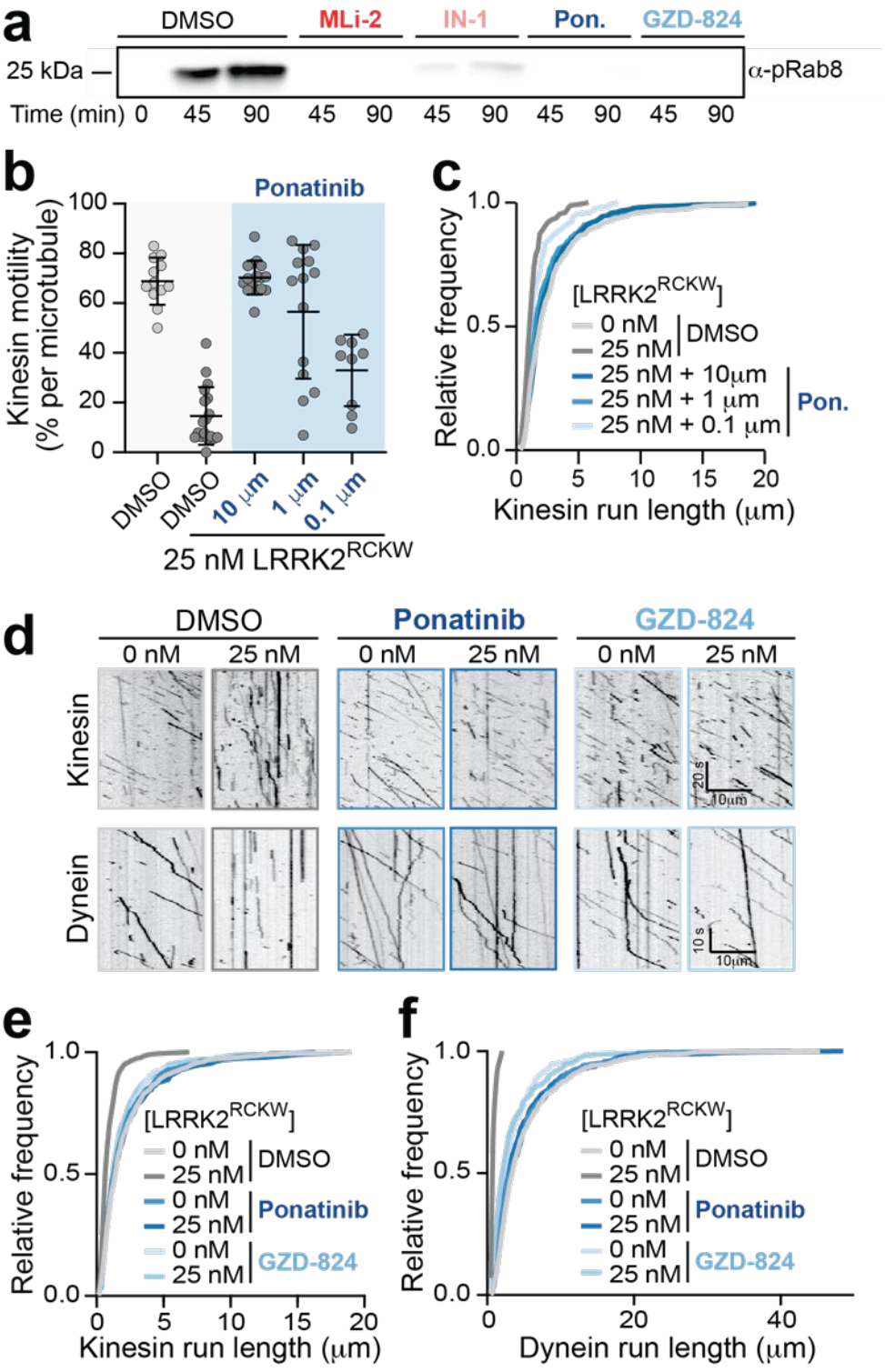
a
DMSO
MLi-2
IN-1
Pon.
GZD-824
25 kDa
α-pRab8
Time (min) 0 45 90 45 90 45 90 45 90 45 90
b
Ponatinib
Kinesin motility (% per microtubule)
100
80
60
40
20
0
DMSO
DMSO
10 μm
1 μm
0.1 μm
25 nM LRRK2RCKW
c
Relative frequency
1.0
0.5
0.0
[LRRK2RCKW]
0 nM
25 nM
DMSO
25 nM + 10μm
25 nM + 1 μm
25 nM + 0.1 μm
Pon.
0 5 10 15 20
Kinesin run length (μm)
d
DMSO
Ponatinib
GZD-824
0 nM
25 nM
Kinesin
Dynein
20 s
10μm
10 s
10μm
e
Relative frequency
1.0
0.5
0.0
[LRRK2RCKW]
0 nM
25 nM
DMSO
0 nM
25 nM
Ponatinib
0 nM
25 nM
GZD-824
0 5 10 15 20
Kinesin run length (μm)
f
Relative frequency
1.0
0.5
0.0
[LRRK2RCKW]
0 nM
25 nM
DMSO
0 nM
25 nM
Ponatinib
0 nM
25 nM
GZD-824
0 20 40
Dynein run length (μm)

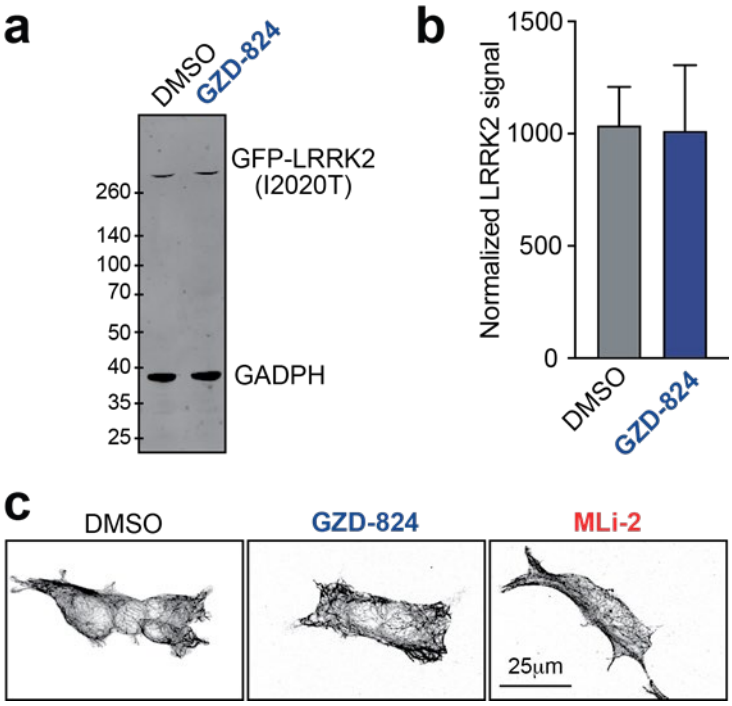

Extended Data Figure 16 | Microtubule architecture and LRRK2 expression are not perturbed by kinase inhibitors. a, Expression levels of GFP-LRRK2 (I2020T) in 293T cells treated with either DMSO or GZD-824 (5 µM). An Immunoblot with anti-GFP (LRRK2) and anti-GADPH (loading control), which is a representative image from three replicates, is shown. **b**, Quantification of GFP-LRRK2 (I2020T) expression levels from Western blots similar to (a). Data are mean ± s.d. (n = 3 per condition). GZD-824 is not significantly different from the DMSO-treated control (Mann-Whitney test). **c**, 293T cells immunostained for tubulin showing that the microtubule architecture is not affected by GZD-824 or MLi-2 compared to DMSO treatment. See Extended Data Table 1 for all source data and replicate information.